THE ASTROPHYSICAL JOURNAL, 449:592–615, 1995 August 20

THE PLANETARY NEBULA SYSTEM AND DYNAMICS OF NGC 5128. III. KINEMATICS AND HALO MASS DISTRIBUTIONS

XIAOHUI HUI,[1,2,3,4,5] HOLLAND C. FORD,[2,5,6] KENNETH C. FREEMAN,[7] AND MICHAEL A. DOPITA[7]
Received 1994 December 3; accepted 1995 March 2

ABSTRACT

We present a study of the halo dynamics and mass distributions of the nearby giant elliptical galaxy NGC 5128 using planetary nebulae (PNs) as test particles. Radial velocities of 433 PNs were obtained with multifiber spectrographs on both the Anglo-Australian Telescope (AAT) and the Cerro Tololo Inter-American Observatory (CTIO) 4 m telescope. The velocities were measured from the [O III] λ5007 emission line with a typical 1 σ error of ± 4 km s^{-1} and ± 30 km s^{-1} for the AAT and the CTIO data, respectively. These PNs cover the entire galaxy to a radius of 10 kpc and extend along the photometric major axis out to 20 kpc.

The PN velocity field shows the distinctive characteristics of a triaxial potential: the galaxy's rotation axis is offset from its photometric minor axis by $39° \pm 10°$; the rotation axis and the line of maximum rotation are likely not orthogonal. We also find that the ordered motions of the stars become more important with increasing radius compared to their random motions. The rotation reaches approximately 100 km s^{-1} and 50 km s^{-1} along the photometric major and minor axes, giving a local V/σ ratio of about 1.0 and 0.5, respectively. The aximuthal variation of the velocity dispersion appears to be modulated by rotation, i.e., it reaches a maximum where the largest rotation is observed and drops to a minimum at zero rotation. The amplitude of this modulation is about 20 km s^{-1}, compared to a mean dispersion velocity of 110 km s^{-1}.

The kinematics of the globular clusters depend on the metallicity. Taking [Fe/H] $= -1.0$ as the dividing point, the metal-poor clusters do not show any significant rotation. However, the metal-rich clusters show both major and minor axis rotation, and the amplitudes of the rotation are similar to that of the PNs.

The stellar velocity dispersion measured from absorption-line spectra together with an Hα rotation curve of the dust lane suggest that the stellar orbits are isotropic and the mass-to-light ratio (M/L_B) is 3.9 in the central region of the galaxy. By applying the isotropic Jeans equation to the observed PN major axis rotation and velocity dispersion, we show that the M/L_B increases with radius, suggesting the presence of dark matter in the halo. Within a 25 kpc radius, the total mass of the galaxy is $3.1 \times 10^{11}\ M_\odot$ and $M/L_B = 10$. The rotation velocity of the recently detected H I ring at a radius of 15 kpc confirms our mass model.

The misalignment of the rotation axis relative to the photometric minor axis, combined with the knowledge of the dust lane orientation, allows us to uniquely determine the observer's viewing direction. The true shape of the galaxy is nearly spherical yet sufficiently triaxial to impose a distinctive gravitational signature on the kinematics.

Subject headings: galaxies: abundances — galaxies: individual (NGC 5128) — galaxies: kinematics and dynamics — galaxies: star clusters

1. INTRODUCTION

The current dynamical states of galaxies provide important clues to their formation and evolution history. However, for elliptical galaxies, as well as the bulges and halos of spiral galaxies, our knowledge of their stellar kinematics is hampered by observations. Usually, stellar velocities are measured from integrated light. The rapid falloff in surface brightness limits such measurements to the bright central regions. In fact, most of the absorption spectrum data only reach approximately one effective radius (r_e) (Illingworth 1977; Davies et al. 1983; Franx, Illingworth, & Heckman 1989). Little is known about the stellar kinematics in the halos of early-type galaxies.

Planetary nebulae (PNs) are excellent test particles for probing the halo dynamics in early-type galaxies. They are stars evolving from the asymptotic giant branch (AGB) to their final destiny, white dwarfs. Since a majority of stars of 1 to 8 solar masses evolve through the PN phase, in an old population, such as in elliptical galaxies, many stars are currently in the PN phase. The central stars of PNs are as hot as O stars and as bright as red supergiants. Although most of their luminosity is in the UV, the nebular shells convert the UV ionizing photons into various line emissions in the infrared, optical, and UV. Among them, up to 15% of the central star's energy are reemitted in the [O III] λ5007 line, the brightest optical emission line of a PN (Dopita, Jacoby, & Vassiliadis 1992). Because of this high concentration of energy in a single emission line, PNs are observable with a narrow bandwidth interference filter in distant galaxies. With 4 m class telescopes, several hundred PNs can be identified in individual galaxies up to 15 Mpc. After a nebula is identified, only a few hundred photon counts are needed in a high dispersion spectrum to measure its velocity to an accuracy of 15 km s^{-1}. With multiobject

[1] Astronomy Department, Boston University, Boston, MA 02215.
[2] Physics and Astronomy Department, Johns Hopkins University, Baltimore, MD 21218.
[3] Hubble Fellow.
[4] Astronomy Department, California Institute of Technology, Pasadena, CA 91125.
[5] Visiting astronomer, Cerro Tololo Inter-American Observatory, operated by the Association of Universities for Research in Astronomy, Inc., under contract with the National Science Foundation.
[6] Space Telescope Science Institute, Baltimore, MD 21218.
[7] Mount Stromlo Observatory, Canberra, ACT, Australia.

spectrographs, radial velocities of 50 to 100 nebulae can be obtained in a single night.

By observing PNs, kinematical information in the halo of early-type galaxies can be obtained to at least 20 kpc. This allows us to use the stellar kinematics to explore the halo mass distribution in these galaxies. Unlike spiral galaxies where extended flat H I rotation curves provide strong evidence for dark matter, no practical dynamical tracers were available in the outer halos of elliptical galaxies before the PN observations. Although mass distribution studies are complicated by stellar orbits in any dynamically hot systems, in a constant mass-to-light ratio model, the stellar velocities will eventually decrease. Substantial evidence can be placed on the dark matter when velocities are measured to a large radius. Recent work by Saglia et al. (1993) showed that flat or slowly rising velocity dispersion profiles extending to $1–2r_e$ indicate the presence of dark matter in the three elliptical galaxies studied.

Halo stellar kinematics will also help us better understand the formation and evolution of elliptical galaxies. Recently, Hernquist (1993) carried out a numerical simulation study of mergers between two identical galaxies consisting of a self-gravitating disk, bulge, and halo. His experiments suggested that while elliptical galaxies formed by major mergers have little rotation in the center, the outlying regions rotate rapidly. The rotation velocity could reach the local velocity dispersion at radii $r \geq 2–3r_e$. PN velocities can be measured to at least $4r_e$, and thus the stellar kinematics at large radii can be compared directly with the numerical models. Furthermore, the halo PNs are in the same radius range as globular clusters. Studies of both stars and clusters will help discriminate among formation scenarios such as dissipative collapse, mergers of primeval galaxies, or low-redshift mergers.

NGC 5128 (also a radio source, Centaurus A) is a giant elliptical galaxy with a prominent dust lane lying along its photometric minor axis. For a long time, it was considered to be a peculiar galaxy. With the discovery of dust lanes in many other galaxies, NGC 5128 is now recognized as a prototype of objects resulting from a merger of two galaxies. These galaxies are characterized by an elliptical stellar body bisected by a rotating disk of gas and dust (Bertola 1987). Because disks tend to settle into certain preferred planes of an elliptical potential (Merritt & de Zeeuw 1983), they can be used along with the stellar kinematics to explore the structure of elliptical galaxies. As the closest of dust lane galaxies, NGC 5128 has been observed extensively and provides an excellent laboratory for studying the dynamics and mass distribution of elliptical galaxies.

The nature of the main elliptical component of NGC 5128 was established by spectroscopic and photometric observations (van den Bergh 1976). As early as 1962, Burbidge and Burbidge concluded that the absorption lines in the spectra of the galaxy's main body come from an old stellar population expected for a normal giant elliptical galaxy (Burbidge & Burbidge 1962). The fact that its surface brightness distribution follows de Vaucouleurs's law confirms that the galaxy is an elliptical (van den Bergh 1976; Dufour et al. 1979, hereafter D79).

Because of the low surface brightness in the halo of the galaxy, previous dynamical studies have largely been restricted to observations of the bright envelope and the conspicuous dust lane. Graham (1979) used observations of the discrete H II regions along the edge of the dust lane to show that the gas and dust are in a highly inclined, rotating disk. Subsequent observations of the diffuse H II gas (Bland, Taylor, & Atherton 1987, hereafter BTA) and the H I clouds (van Gorkom et al. 1990) verified Graham's description. Stellar absorption-line studies of the bright envelope by Wilkinson et al. (1986, hereafter WSFW) revealed that stars rotate slowly around the photometric minor axis of the elliptical component, perpendicular to the rotation of the gaseous disk. These studies reinforced the speculation of Baade & Minkowski (1954) that NGC 5128 is two galaxies in collision.

The long-slit observations of WSFW were limited to a few kiloparsecs from the center of the galaxy and mostly to the photometric major axis. In order to make a complete study of the halo dynamics and mass distribution, we surveyed NGC 5128 for PNs with the Cerro Tololo Inter-American Observatory (CTIO) 4 m telescope. In the survey area which extends to 20 kpc along the photometric major axis and covers the whole galaxy to 10 kpc, a total of 785 PNs were identified (Hui et al. 1993a, b, hereafter Paper I and Paper II, respectively). Subsequently, we made extensive efforts to obtain PN spectra with the multifiber spectrographs. Three spectroscopic observing runs, totaling nine useful nights, were carried out on both the Anglo-Australian Telescope (AAT) and the CTIO 4 m telescope. Velocities of 433 PNs were successfully measured.

This paper, the third in the sequence, discusses the details of the spectroscopic observations, examines the properties of the stellar velocity field from the PN data, and studies the structure and mass distribution of the galaxy. The paper is arranged as follows. We present the details of the spectroscopic observations in § 2 and the data reductions in § 3. Then, a catalog of 433 PN velocities is given in § 4. Following the data presentation, we proceed to report the kinematical properties of the NGC 5128 PN system (§ 5). The kinematics of the galaxy's globular cluster system is also compared with that of PNs in this section. In § 6, kinematical information provided by different dynamical tracers, namely, the Hα disk rotation curve, the stellar rotation and velocity dispersion, and the globular cluster velocities, is used to study the mass distribution of the galaxy. Finally, we explore in § 7 the intrinsic shape of the galaxy and the viewing direction of the observer using the knowledge of the dust lane orientation and the misalignment between the stellar rotation axis and the photometric minor axis.

2. SPECTROSCOPIC OBSERVATIONS

2.1. *AAT Observations*

PN spectra were first obtained on the AAT with the multifiber system of the Royal Greenwich Observatory (RGO) spectrograph in 1987 and 1989. The instrument setups are given in Table 1. By using a metal aperture plate, simultaneous exposures of over 50 objects were allowed in a 40′ diameter field of the Cassegrain focus. The spectra were centered around [O III] λ5007 with a wavelength coverage of 4700–5245 Å. Using the 1200 V grating in the first order and the 25 cm camera, the spectral resolution was 0.5 Å per 15 μm channel. The diameter of individual fibers was 320 μm or 2″.1 on the sky, giving an instrumental FWHM of approximately 2 Å.

For each plate, we took four to five 2000 s integrations, sandwiched by exposures of a Ti-Ar lamp. A quartz-lamp flat-field image was also taken for each fiber plate. In total, we were able to observe five plates in 1987 and six plates in 1989. A journal of the observations is given in Table 2.

TABLE 1

THE INSTRUMENT SETUPS

Telescope Date	AAT 1987 April	AAT 1989 March	CTIO 4 m 1989 April
Focal ratio	f/8	f/8	f/2.77
Spectrograph	RGO	RGO	RGO
Camera	25 cm	25 cm	Air Schmidt
Detector	IPCS	IPCS	GEC CCD
e^-/ADU[a]	...	...	1.04
Readout noise	...	...	$7e^-$
Grating	1200 lines mm^{-1}, first	1200 lines mm^{-1}, first	527 lines mm^{-1}, first
Fiber diameter	320 μm, 2".1	320 μm, 2".1	100 μm, 1".8
Dispersion	0.5 Å $pixel^{-1}$	0.5 Å $pixel^{-1}$	1.75 Å $pixel^{-1}$
FWHM	2 Å	2 Å	4 Å
Number of plates	4	6	...
Number of configurations	...	...	19
Number of fibers	55	55	12

[a] Analog-to-digital converter unit.

2.2. *CTIO 4 Meter Observation*

In 1989 April, we used the fiber-fed spectrograph ARGUS on the CTIO 4 m telescope to acquire a third set of PN spectra. The instrument setups are given in Table 1. Using the grating KPGL3 in the first order, the spectral resolution was 1.75 Å per 22 μm pixel of the Griboval electronographic camera (GEC) CCD detector. The 100 μm diameter (1".8) fibers projected into $\sim$2 pixels on the detector and gave an instrumental FWHM of approximately 4 Å. The wavelength coverage of the spectra was from λ4450 to λ5440.

The ARGUS had 12 robot positioners at the time. Each places one fiber onto a specific position at the prime focus of the telescope. The fibers transmit the light to a bench-mounted spectrograph located in an isolated room. Due to the faintness of the PNs, we first centered the fibers on bright reference stars, then moved them onto the nearby PNs. The PNs were grouped into 19 configurations (Table 3). Each configuration typically had one to two 1800 s exposures, depending on the average PN brightness of the group. He-Ar spectra were taken at the beginning and end of each night, as well as two in the middle. Because it was a bench-mounted spectrograph, there was no mechanical flexure when the telescope moved; the spectral shifts in both the dispersion and aperture directions were minimal.

TABLE 2

JOURNAL OF THE AAT OBSERVATIONS

Plate Number	UT Date	Starting H. A.	Number of 2000 s Exposures	Seeing
CENA_5	1987 Apr 30	1^h44^mE	4	2".0
CENA_6	1987 Apr 30	1 03 W	6	2.5
CENA_1	1987 May 1	3 08 E	4	2.5
CENA_5	1987 May 1	0 14 W	3	2.5
CENA_2[a]	1987 May 1	1 54 W	5	3.5
CENA89_6	1989 Mar 8	3 54 E	4	1.8
CENA89_1	1989 Mar 8	1 02 E	5	1.8
CENA89_2	1989 Mar 9	1 58 E	4	1.8
CENA89_3	1989 Mar 9	0 02 W	4	1.8
CENA89_9	1989 Mar 10	3 48 E	4	2.0
CENA89_7	1989 Mar 10	0 44 E	5	1.5

[a] The weak signals on plate CENA_2 did not give useful information owing to poor seeing.

3. DATA REDUCTION AND CALIBRATION

The data reductions consisted of three basic steps. The spectra were first extracted from the images of two-dimensional detectors. Then they were calibrated onto a linear wavelength scale using the comparison spectra. Finally, a Gaussian function was fitted to the [O III] λ5007 line, the only observable line for most PNs, to obtain an accurate velocity for each PN.

3.1. *1987 AAT Spectra*

The 1987 spectra were reduced at the Mount Stromlo Observatory, using a combination of the FIGARO, PANDORA, and STARLINK software packages. We first extracted the spectra from the IPCS frames, using the quartz-lamp flat fields to determine the positions of individual fiber spectra in the frames. Cross-correlating the spectra of the com-

TABLE 3

JOURNAL OF THE CTIO 4 METER OBSERVATIONS

Configuration	UT Date	Starting H.A.	Number of 1800 s Exposures	Seeing
CNAPN3	1989 Apr 4	3^h25^mE	2	1".0
CNAPN1	1989 Apr 4	1 10 E	2	1.0
CNAPN2	1989 Apr 4	0 49 W	2	1.0
CNAPN4	1989 Apr 4	2 15 W	1	1.0
CNAPN3	1989 Apr 4	2 53 W	1	1.0
CNAPN5	1989 Apr 5	3 09 E	1	1.0
CNAPN6	1989 Apr 5	2 26 E	2	1.0
CNAPN7	1989 Apr 5	1 11 E	1	1.0
CNAPN8	1989 Apr 5	1 22 W	2	1.0
CNAPNV1	1989 Apr 5	2 38 E	1	1.0
CNAPNV2	1989 Apr 5	3 17 E	1	1.0
CNAPN9	1989 Apr 5	3 52 W	1	1.0
CNAPN10	1989 Apr 5	2 51 E	1	1.5
CNAPN11	1989 Apr 6	2 07 E	2	1.5
CNAPN9	1989 Apr 6	0 45 E	2	1.5
CNAPN12	1989 Apr 6	0 25 W	2	1.5
CNAPN21	1989 Apr 6	1 52 W	1	1.5
CNAPN1	1989 Apr 6	3 27 E	1	1.5
CNAPN22	1989 Apr 7	4 32 E	1	1.5
CNAPN24	1989 Apr 7	0 25 E	2	1.5
CNAPN22	1989 Apr 7	0 46 W	2	1.5
CNAPN25	1989 Apr 7	2 08 W	2	1.5
CNAPN13	1989 Apr 7	3 21 W	2	1.5

parison lamp from successive exposures showed that the instrumental shifts were small, so we used the means of the comparison spectra before and after each PN frame. Typically, 9 lines of the comparison spectra were fitted by a third-order polynomial. The PN spectra were reduced to a linear wavelength scale fiber by fiber. We checked this procedure by rebinning the comparison spectra onto a linear wavelength scale. In all the cases, the residual shift for each fiber between a comparison spectrum and a reference was less than 3 km s^{-1}, estimated by cross-correlation. Finally, we added together the exposures of the same plate.

The [O III] λ5007 line profiles were modeled using the Gaussian fitting routines of the SPECTRE code (Pelat, Alloin, & Fosbury 1981). The spectra were smoothed with a Gaussian of $\sigma = 1$ pixel before the fitting. The program minimizes the χ^2 function by adjusting simultaneously the central wavelength, the peak, and the FWHM of each line. The fitting processes were monitored by displaying each spectrum. Spectra with only noise were recorded and deleted.

3.2. *1989 AAT and CTIO 4 Meter Spectra*

The 1989 AAT and CTIO spectra were reduced using the IRAF package. The calibration procedures for the AAT data were similar to those described above. We extracted the individual spectra from the images using the quartz-lamp flat-field frames as the template. By identifying 4 lines on every exposure of the comparison lamp, the spectral shifts were estimated to be small ($\sim$0.1 Å) between successive exposures. Therefore, the PN spectra were reduced to a linear wavelength scale using the sum of the comparison spectra taken before and after each exposure. The spectral solutions were obtained by fitting a third-order Chebyshev polynomial function to typically 10 lines. The exposures for the same plate were summed after the wavelength calibration.

The CCD images from the CTIO run were trimmed and bias subtracted. The bench-mounted spectrograph made the spectral shift minimal, so we started by adding together the successive exposures of the same configuration. The spectra of individual fibers were then extracted according to the fiber positions determined on the quartz-lamp image taken at the beginning of each night. Every night, four Helium-Argon comparison spectra were obtained. However, careful examination showed that no significant spectral shift was present in the spectra of the same night. Consequently, only the one taken at the beginning of each night was used to calibrate the PN spectra to a linear scale. Either a fourth- or a fifth-order Chebyshev polynomial were used to fit 9 to 11 lines to obtain the spectral solutions.

The program SPECTRE was used to fit a Gaussian function to the [O III] λ5007 lines. The AAT data were convolved with a Gaussian of $\sigma = 1$ pixel. However, the CTIO spectra were not smoothed since it would further broaden the 4 Å FWHM lines. The fitting of individual PN spectra was monitored, and spectra with only noise or a distorted line profile were discarded. Some typical spectra with different line strengths are shown in Figure 1 for the 1989 AAT data and in Figure 2 for the CTIO data.

3.3. *Velocity Accuracy*

The PN velocities were checked extensively by comparing the repeated measurements. In the 1987 AAT run, plate CENA_5 was observed twice in consecutive nights. Additionally, about 10 PNs were on both plates CENA_6 and CENA_1. In Figure 3 the velocity differences of these PNs are plotted against the minimum photon counts of the two measurements. No systematic offset is present between the two velocity sets. The estimated 1 σ error σ_V as a function of photon counts is given in Table 4, where $\sigma_{\Delta V}$ is the rms of the velocity differences. The velocity error, σ_V, is bounded by an upper limit, $\sigma_{\Delta V}$, if the velocities with higher counts have negligible errors and a lower limit, $\sigma_{\Delta V}/(2)^{1/2}$, if the velocity uncertainties are the same for the two measurements. Combining this with Figure 4*a*, an accumulative photon counts distribution, we conclude that at least 65% of the 1987 AAT velocities are accurate to ± 4 km s^{-1}. Although few PNs have two measurements for the 1989 AAT run, with the same instrument setting and observing procedure, we expect that the internal errors are similar. Hence, about 75% of the AAT 1989 PNs with 100 counts or more (Fig. 4*b*) should have a velocity accuracy of ± 4 km s^{-1}.

Because the readout noise is significant in the CTIO spectra, the CTIO velocities have lower accuracy than the AAT ones at the same photon counts. In the latter case, the IPCS is a noise-free detector. Based on 14 pairs of double measurements (Fig. 5*a*), the velocity uncertainty of the CTIO data is estimated to be 42 km $s^{-1} > \sigma_V >$ 29 km s^{-1} between 100 and 400 counts. During the CTIO run, we planned two configurations to overlap with the AAT data. Figure 5*b* plots the velocity differences of the two data sets against the CTIO counts. Since the error of the AAT velocities is much smaller than that of the CTIO data, this provides another accuracy estimate of the CTIO velocities. The resulting 1 σ error is ± 23 km s^{-1} for PNs with over 400 counts, and ± 34 km s^{-1} for PNs with fewer counts. Thus, the two estimates are consistent. Given the counts level (Fig. 6), the typical velocity error is approximately 30 km s^{-1} for the CTIO data.

Using Figure 5*b*, we also estimate that the systematic velocity difference is 6.7 ± 7.8 km s^{-1} between the CTIO and the AAT 1987 data, and -14.5 ± 8.4 km s^{-1} between the CTIO and the AAT 1989 data. Given the uncertainties, the offsets do not seem to be significant.

4. NGC 5128 PLANETARY NEBULA VELOCITY CATALOG

The three data sets are merged to yield a catalog of 433 PN velocities (Table 5). In the table, column (1) gives the PN identification, which is the same as in Table 1 of Paper II; column (2) gives the PN velocity in kilometers per second; column (3) gives the galactic radius in arcminutes; column (4) gives the photometric major axis distance (X), positive to the northeast; column (5) gives the photometric minor axis distance (Y), positive to the northwest; column (6) gives the PN m_{5007} magnitude (Paper II); column (7) gives the total analog-to-digital counts in the [O III] λ5007 line; column (8) gives the FWHM of the line; and column (9) is 1 for the 1987 AAT run, 2 for the 1989 AAT run, and 3 for the 1989 CTIO run. For PNs with

TABLE 4

ESTIMATED VELOCITY ERRORS FOR THE AAT 1987 DATA

Counts (photons)	$\sigma_{\Delta V}$ (km s^{-1})	σ_V (km s^{-1})
≥ 100	5	$5 > \sigma > 3$
50–100.....	12	$12 > \sigma > 8$
≤ 50	19	$19 > \sigma > 13$

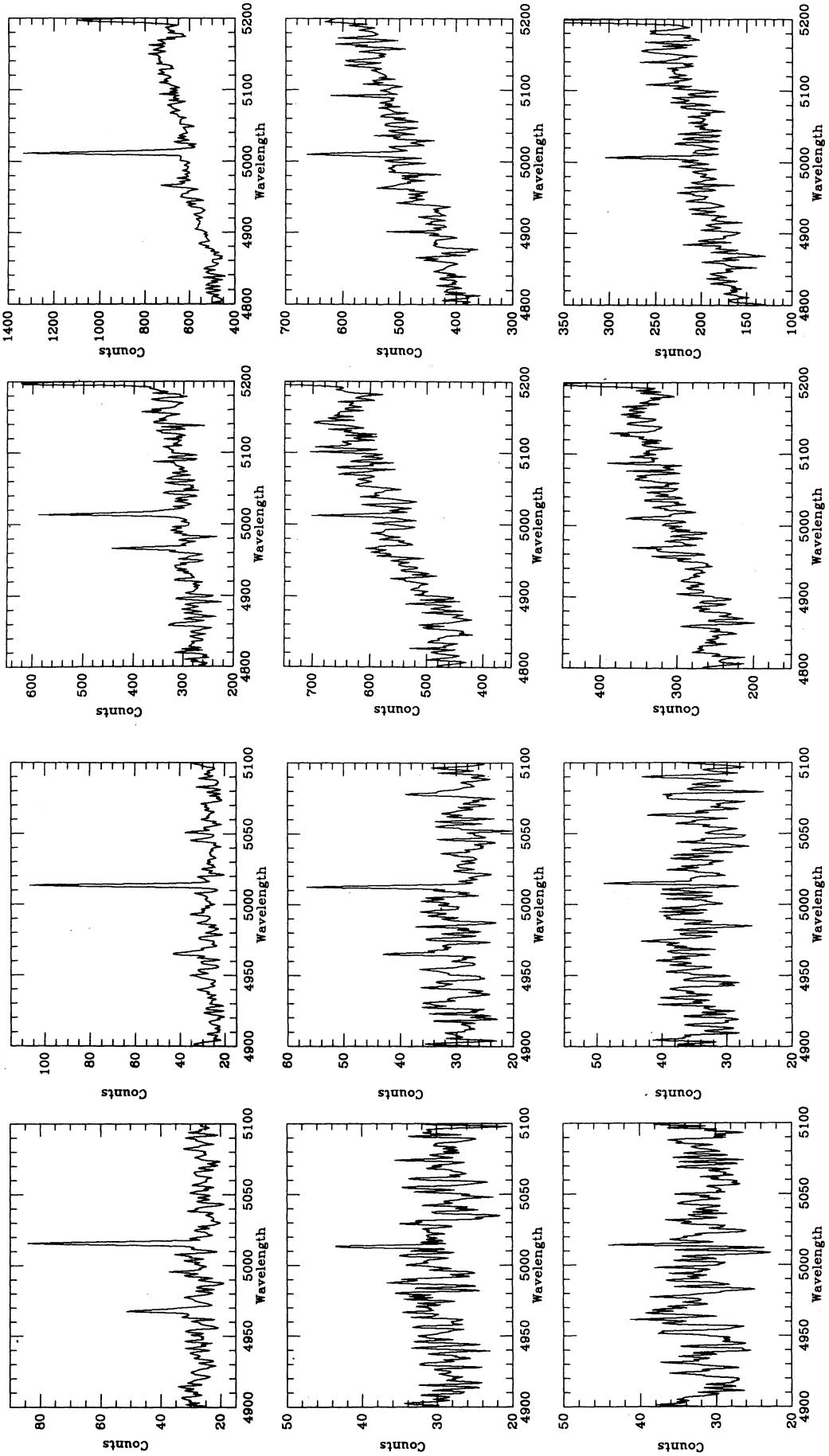

FIG. 1

FIG. 1.—Examples of the spectra obtained during the AAT 1989 observation. The spectra were convolved with a Gaussian of $\sigma = 1$ pixel.

FIG. 2.—A collection of the CTIO [O III] λ5007 line profiles. No smoothing was applied.

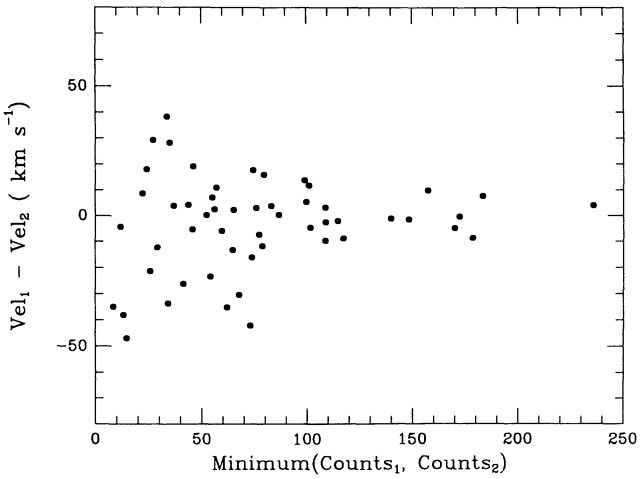

FIG. 3.—The velocity differences of the two measurements are plotted against the minimum photon counts of the two for the 1987 AAT data.

repeated measurements, their velocities are the count-weighted averages if the measurements were obtained in the same run, and they are the simple averages otherwise.

In calculating the coordinates (X, Y), the galactic center is assumed at

$$\alpha(2000) = 13^{h}25^{m}27^{s}.72 ,$$

$$\delta(2000) = -43°01'5''.8$$

(Kunkel & Bradt 1971), and the photometric major axis at P.A. = 35° (D79). The (X, Y) presented are sufficiently accurate that the full precision of the PN coordinates can be recovered.

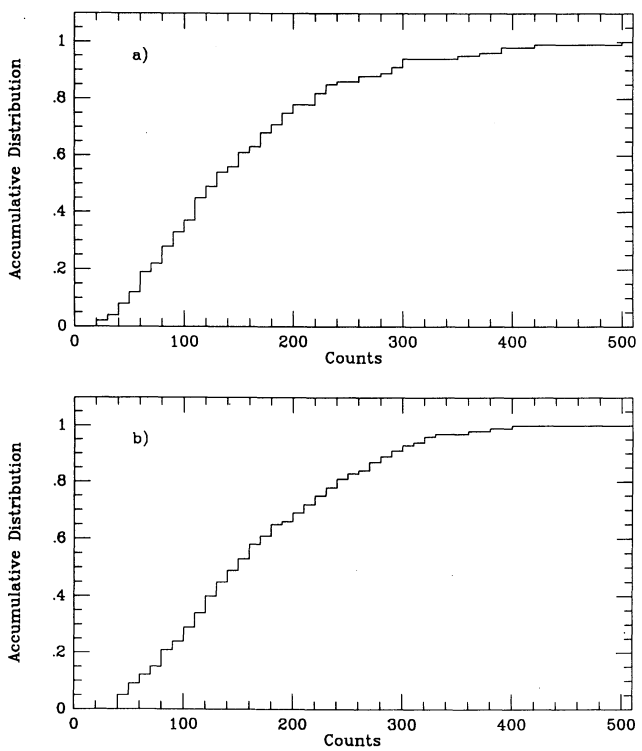

FIG. 4.—(*a*) Accumulative photon counts distribution of the AAT 1987 data. (*b*) Accumulative photon counts distribution for the AAT 1989 data.

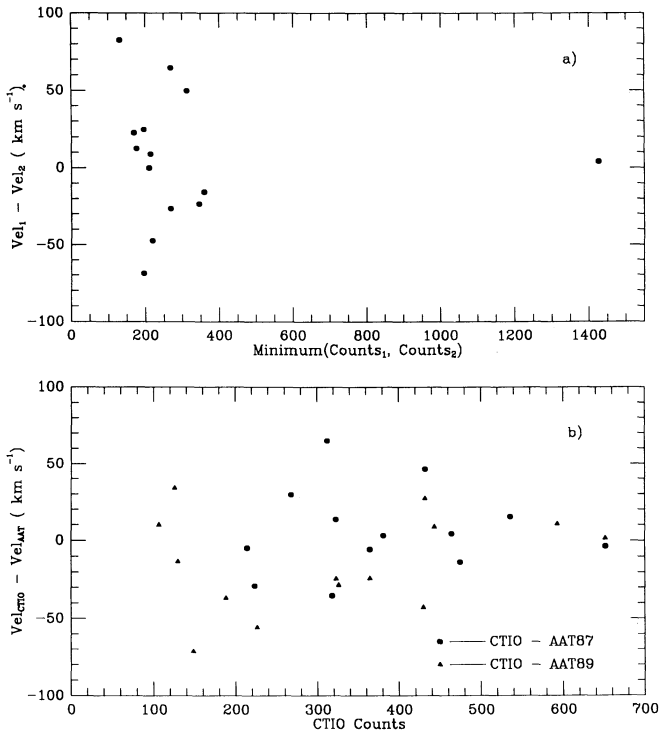

FIG. 5.—(*a*) The velocity differences of the two measurements are plotted against the minimum counts of the two for the CTIO data. Among 14 data points, 13 are PNs, and the one with the highest counts is an H II region. (*b*) The AAT and CTIO velocities are compared and the differences are plotted against the CTIO counts.

5. KINEMATICS OF THE PLANETARY NEBULA SYSTEM

5.1. *Systematic Velocity*

In Figure 7, the velocities of all 433 PNs are plotted against their distance to the true rotation axis (see § 5.4). A systematic velocity of 541 ± 7 km s^{-1} is then derived by fitting a straight line to the data. The value agrees satisfactorily with WSFW's 538 ± 10 km s^{-1} derived from absorption spectra, and BTA's 536 ± 5 km s^{-1} derived from emission lines of the rotating disk. The agreement shows that there is little relative motion among various components.

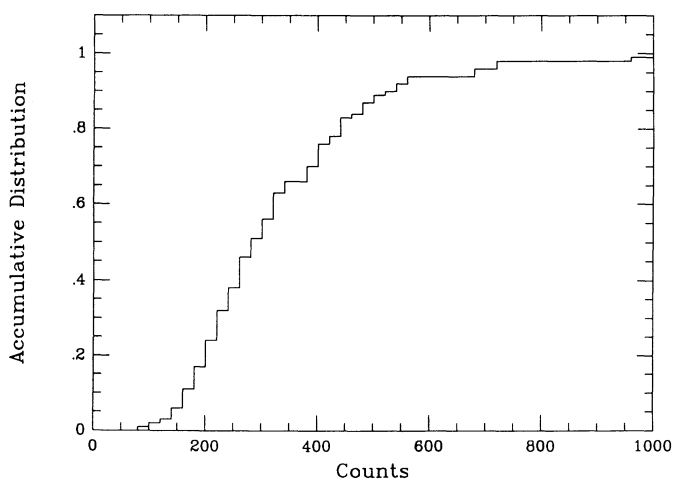

FIG. 6.—Accumulative counts distribution for the CTIO 1989 data

TABLE 5

NGC 5128 PLANETARY NEBULA VELOCITY CATALOG

ID	V	R	X	Y	m_{5007}	Counts	FWHM	Run	ID	V	R	X	Y	m_{5007}	Counts	FWHM	Run
201	684	1.946	1.271	−1.474	23.77	233	4.5	1	2301	604	19.999	−19.966	−1.154	24.86	150	6.5	1
202	431	2.697	1.502	−2.240	23.85	267	3.6	1	2302	671	19.594	−19.358	−3.027	25.39	115	5.0	1
203	491	2.515	0.754	−2.400	23.93	221	4.4	1	2306	687	18.721	−18.097	−4.795	24.68	158	4.6	1
205	546	1.475	0.918	−1.154	24.13	373	5.3	1	2401	333	19.794	−19.199	−4.814	25.35	62	4.8	1
207	475	3.835	2.980	−2.414	24.20	171	3.6	1	2502	537	19.596	−18.767	5.638	24.61	189	4.4	1
210	718	2.576	2.127	−1.453	24.26	234	4.3	1	2503	812	19.832	−19.346	4.364	25.01	161	4.1	1
213	716	1.284	0.465	−1.197	24.30	200	3.6	1	2504	689	19.013	−18.253	5.319	25.88	28	3.3	1
217	460	2.177	0.921	−1.973	24.51	299	9.0	1	2601	685	18.481	−18.476	0.427	24.46	224	4.6	1
504	601	4.589	−2.628	3.762	24.47	111	3.9	1	2602	772	18.437	−18.437	0.079	24.83	177	4.4	1
508	662	1.991	−1.478	1.334	24.69	233	6.4	1	2603	597	17.652	−17.612	−1.182	25.25	125	4.1	1
510	459	1.819	−1.708	0.623	24.75	115	3.2	1	2606	687	17.501	−17.378	−2.068	24.38	246	4.7	1
513	450	3.835	−2.399	2.992	24.80	139	5.1	1	2607	643	16.202	−16.058	−2.156	24.95	225	5.2	1
525	779	2.352	−1.969	1.286	24.98	127	3.5	1	2701	782	24.594	−24.594	0.009	24.63	300	4.5	1
527	679	2.954	−2.402	1.720	24.99	175	4.4	1	2703	682	22.450	−22.450	−0.037	25.66	46	3.4	1
901	524	8.393	6.873	4.818	24.07	308	3.8	1	2704	611	20.520	−20.388	−2.324	24.30	264	4.2	1
902	542	8.346	5.756	6.043	24.26	356	4.5	1	2801	572	23.961	−23.131	6.250	25.12	138	4.5	1
904	539	8.793	5.766	6.638	24.31	153	4.0	1	2802	406	23.571	−22.645	6.541	25.47	48	4.5	1
905	557	7.729	5.619	5.307	24.62	197	4.2	1	2805	612	20.735	−20.354	3.956	25.81	44	3.7	1
906	460	7.030	6.231	3.256	24.64	104	3.9	1	2901	749	17.311	−17.261	1.315	26.10	111	4.4	1
907	522	8.915	7.095	5.399	24.67	72	5.2	1	3001	837	16.348	−15.692	−4.585	24.47	286	4.4	1
908	568	8.893	7.041	5.432	24.93	85	3.8	1	3002	126	16.262	−15.224	−5.719	24.75	137	3.5	1
909	562	7.244	5.118	5.128	24.98	90	4.0	1	3003	708	16.040	−15.329	−4.725	24.51	396	4.8	1
913	451	7.215	4.483	5.653	25.30	56	4.8	1	3004	652	16.941	−15.724	−6.306	25.26	123	5.6	1
914	486	6.975	4.694	5.160	25.36	37	4.1	1	3301	498	21.782	21.736	1.409	24.54	157	4.0	1
915	464	8.152	7.220	3.784	25.59	35	3.5	1	3302	570	22.346	22.286	1.630	25.47	94	6.0	1
916	533	8.155	4.785	6.603	25.59	66	5.1	1	3401	575	15.465	−15.366	1.743	24.85	173	5.5	1
1001	686	10.933	7.200	8.228	24.16	428	4.0	1	3402	680	14.434	−14.422	0.578	24.72	285	4.3	1
1002	496	10.117	8.279	5.814	24.85	161	3.8	1	3403	642	15.077	−14.983	−1.681	24.13	222	4.0	1
1003	470	11.940	8.529	8.356	24.86	114	3.2	1	3405	827	13.439	−13.418	−0.756	25.51	158	4.4	1
1004	742	12.118	8.203	8.920	25.24	84	4.8	1	3501	385	14.257	−13.767	3.706	24.22	200	4.3	1
1204	479	8.364	8.210	1.598	24.22	392	4.4	1	3504	515	13.108	−13.082	0.826	24.86	150	4.4	1
1205	619	9.274	9.231	−0.895	24.31	296	4.0	1	3505	885	12.936	−12.933	0.273	24.84	203	4.3	1
1208	650	9.057	8.486	3.167	24.89	79	6.0	1	3506	664	12.290	−12.287	0.244	25.19	97	3.7	1
1211	583	9.908	9.902	0.351	24.98	62	4.6	1	3507	615	11.019	−11.019	0.028	24.95	66	3.5	1
1213	460	8.592	8.486	1.346	25.10	103	4.9	1	3510	859	11.386	−11.360	0.773	25.74	91	4.4	1
1214	505	8.184	7.602	3.032	25.15	310	3.7	1	4001	398	7.137	6.896	1.837	23.89	—	—	1,3
1216	498	8.707	8.431	2.175	25.41	58	3.9	1	4002	335	7.325	7.259	0.987	24.04	299	1.8	3
1217	522	10.190	10.169	−0.663	25.43	105	4.0	1	4004	476	6.315	6.315	−0.032	24.23	224	1.8	3
1301	393	10.200	9.926	2.346	24.13	196	3.6	1	4005	290	5.494	5.422	−0.889	24.29	690	2.2	3
1302	419	10.053	10.003	1.005	24.28	164	5.1	1	4006	480	6.093	5.797	−1.877	24.41	263	3.2	3
1303	524	11.770	11.769	−0.172	24.42	102	3.6	1	4008	402	7.246	7.167	−1.067	24.49	168	1.6	3
1304	400	9.335	9.169	1.750	25.13	113	6.5	1	4009	312	4.815	4.783	−0.554	24.63	574	2.5	3
1305	402	11.555	11.504	−1.085	25.21	50	5.7	1	4011	387	6.173	5.952	−1.639	24.59	259	1.8	3
1306	588	12.340	12.290	1.112	25.30	87	4.0	1	4012	783	6.612	6.558	−0.842	24.68	484	2.3	3
1307	582	10.301	10.290	0.459	25.43	62	6.8	1	4015	418	7.451	7.428	−0.586	24.69	127	1.9	3
1308	657	11.885	11.868	0.642	25.53	26	3.1	1	4016	648	5.851	5.632	−1.586	24.73	146	4.8	2
1401	475	14.013	13.933	−1.501	24.12	508	4.2	1	4018	385	5.801	5.764	−0.654	24.72	428	3.0	3
1402	535	14.879	14.863	−0.710	24.70	82	4.4	1	4019	545	7.880	7.798	1.131	24.80	90	5.4	1
1403	604	13.642	13.567	1.425	24.74	185	4.7	1	4022	354	5.943	5.714	−1.636	25.00	60	3.6	2
1404	371	14.111	14.110	−0.178	25.24	119	5.1	1	4023	209	8.051	8.042	0.381	25.09	124	5.5	1
1502	499	16.494	16.465	−0.985	24.50	197	3.7	1	4024	542	5.006	4.947	−0.760	25.09	409	1.8	3
1601	349	18.471	18.471	−0.085	23.98	137	5.6	1	4025	268	4.867	4.790	−0.861	25.12	146	7.2	2
1701	500	17.924	17.238	4.910	24.73	73	3.4	1	4031	497	8.981	8.979	−0.215	25.81	45	3.2	1
1901	440	15.824	15.235	−4.275	24.81	84	3.7	1	4103	604	3.936	3.678	1.402	23.65	476	2.1	3
1902	417	17.661	17.112	−4.368	24.01	144	4.3	1	4104	424	2.425	2.401	0.336	23.76	290	1.9	3
1903	305	19.264	18.642	−4.857	24.19	130	4.4	1	4106	286	2.369	2.247	−0.751	23.83	—	—	1,3
2001	570	15.830	15.581	2.800	24.57	209	4.0	1	4108	426	3.012	2.482	1.706	23.91	356	3.1	3
2002	447	16.335	15.823	4.058	25.23	63	4.7	1	4110	336	2.028	1.969	−0.486	24.06	143	1.9	3
2003	446	14.962	14.919	1.133	24.35	173	4.4	1	4111	554	2.937	2.272	1.860	24.18	422	2.8	3
2004	460	16.392	16.307	1.662	25.10	98	5.1	1	4112	431	2.202	2.162	0.419	24.04	1890	2.5	3
2101	703	20.439	−20.365	1.733	25.65	116	4.9	1	4115	554	2.301	2.287	−0.245	24.20	323	5.9	2
2102	624	20.299	−20.297	0.342	25.52	56	3.2	1	4117	405	4.130	4.117	−0.320	24.06	168	2.0	3
2204	682	19.882	−19.513	3.811	25.90	70	4.3	1	4120	656	3.129	2.468	1.924	24.35	263	4.5	2
2206	420	19.516	−19.349	2.547	25.10	67	5.0	1	4121	503	2.770	2.027	1.888	24.30	194	5.0	2
2207	886	19.505	−19.453	1.423	25.58	187	5.5	1	4122	816	2.650	2.480	−0.934	24.24	691	2.3	3
2208	711	19.553	−19.539	0.734	25.00	114	3.4	1	4123	598	2.503	2.502	−0.066	24.30	309	2.7	3

TABLE 5—*Continued*

ID	V	R	X	Y	m_{5007}	Counts	FWHM	Run
4124	328	3.304	3.288	−0.329	24.28	185	2.2	3
4125	545	2.061	1.993	−0.523	24.35	82	3.1	2
4126	387	1.521	1.483	−0.337	24.36	—	—	1,3
4127	417	3.339	3.137	1.142	24.48	325	2.0	3
4128	862	2.505	2.127	1.324	24.37	152	4.5	2
4131	442	2.365	2.350	−0.273	24.50	155	9.8	2
4132	654	3.475	2.717	2.167	24.57	217	3.1	3
4133	371	4.177	4.062	0.972	24.59	207	4.6	2
4134	338	3.265	2.755	−1.752	24.32	—	—	1,3
4135	439	4.016	3.893	0.987	24.32	—	—	2,3
4136	645	2.263	2.086	0.877	24.56	166	5.3	2
4138	384	2.830	2.711	0.812	24.53	289	5.8	2
4140	519	4.029	3.061	2.620	24.47	455	2.5	3
4142	700	2.001	1.945	−0.471	24.09	277	2.2	3
4143	634	1.835	0.874	1.614	24.58	500	3.4	3
4144	557	1.698	1.460	0.867	24.54	231	2.2	3
4146	581	3.979	3.959	0.404	24.39	449	3.0	3
4147	409	3.531	3.530	0.110	24.64	—	—	2,3
4150	548	1.939	1.930	−0.185	24.71	132	3.3	2
4152	579	1.990	1.812	0.824	24.90	90	3.4	2
4153	405	2.469	2.423	0.470	24.66	132	5.1	2
4154	454	1.821	1.794	−0.311	24.64	202	—	3
4155	486	1.679	1.652	−0.302	24.71	—	—	3,3
4156	569	2.101	1.867	−0.964	24.79	161	—	3
4158	605	2.827	2.607	−1.093	24.72	162	5.3	2
4160	415	2.643	2.443	−1.009	24.67	417	2.0	3
4161	772	1.720	0.799	1.523	24.78	209	7.1	2
4162	743	2.371	1.581	1.767	24.48	—	—	2,3
4163	675	3.376	3.247	−0.925	24.91	270	2.2	3
4165	383	2.169	1.596	1.469	24.93	397	3.1	3
4166	567	2.968	1.842	2.327	24.71	296	2.4	3
4167	502	2.230	1.842	1.258	24.94	206	4.6	2
4169	527	2.771	2.448	−1.298	24.69	269	2.2	3
4170	408	2.276	2.158	0.724	24.95	85	4.0	2
4171	816	3.543	3.448	0.814	25.25	121	4.4	2
4172	197	3.942	3.871	0.744	24.95	478	1.9	3
4173	567	2.304	1.490	1.757	25.07	—	—	2,3
4174	550	2.240	2.210	−0.367	24.96	324	2.4	3
4175	336	4.412	4.165	1.455	24.88	165	2.1	3
4176	446	3.181	2.740	1.616	25.04	128	3.8	2
4177	539	3.520	2.330	2.638	25.31	83	3.9	2
4178	390	4.100	4.058	0.591	25.31	302	2.0	3
4180	568	3.784	3.682	0.873	25.47	80	4.0	2
4181	524	3.045	3.032	−0.283	25.21	—	—	2,3
4182	605	3.919	3.765	1.088	25.09	149	2.5	3
4191	585	2.448	1.995	1.419	25.96	197	2.0	3
4204	645	3.620	−3.620	−0.012	23.71	524	4.9	2
4205	447	2.820	−2.698	−0.820	23.80	360	4.8	2
4206	599	2.477	−2.423	−0.515	23.90	289	5.1	2
4207	527	1.943	−1.916	−0.327	24.08	271	4.2	2
4208	765	4.564	−4.561	−0.171	24.15	312	5.2	2
4209	675	1.914	−1.907	−0.171	24.19	240	4.7	2
4210	685	2.110	−2.006	0.656	24.19	295	4.8	2
4211	344	3.647	−3.408	1.297	24.21	279	5.2	2
4212	277	1.974	−1.685	−1.029	24.23	247	4.8	2
4213	732	4.365	−4.178	−1.263	24.22	235	5.3	2
4214	624	3.009	−2.919	0.732	24.27	325	4.4	2
4215	614	5.187	−5.136	0.725	24.29	262	4.8	2
4216	645	4.282	−4.280	0.134	24.32	280	4.7	2
4217	625	4.359	−3.883	1.982	24.29	294	5.2	2
4218	524	5.426	−5.345	0.933	24.33	127	3.6	2
4219	866	4.177	−4.070	0.938	24.32	259	4.4	2
4220	627	2.735	−2.731	−0.154	24.40	97	3.9	2
4221	633	4.440	−4.272	1.208	24.35	106	4.4	2
4222	523	3.699	−3.696	−0.156	24.40	169	4.9	2
4223	822	2.606	−2.386	1.047	24.38	—	—	1,2,3
4224	513	2.243	−2.118	0.738	24.46	—	—	1,2,3
4225	634	2.493	−2.374	−0.762	24.45	527	2.2	3
4226	714	1.452	−1.451	0.052	24.48	125	3.7	2
4227	535	2.106	−1.820	−1.059	24.51	107	3.2	2
4228	684	2.534	−2.412	−0.778	24.52	235	4.5	2
4229	575	5.502	−5.496	0.243	24.55	174	4.5	2
4230	529	2.294	−2.267	−0.355	24.61	236	2.3	3
4231	440	2.865	−2.723	0.889	24.64	210	3.5	3
4232	679	2.922	−2.793	0.861	24.71	449	2.4	3
4233	816	4.003	−3.247	2.341	24.66	226	4.3	2
4234	708	2.748	−2.519	−1.098	24.74	131	4.4	2
4235	642	2.282	−2.160	−0.737	24.72	96	4.5	2
4236	565	3.259	−3.257	0.098	24.75	154	4.0	2
4237	512	4.247	−3.475	2.442	24.74	—	—	1,2,3
4238	687	1.700	−1.649	−0.415	24.69	270	2.1	3
4240	503	5.345	−5.226	−1.118	24.82	163	4.8	2
4241	520	4.629	−4.585	−0.633	24.80	158	3.7	2
4242	742	3.655	−3.566	0.802	24.80	157	5.0	2
4244	469	3.726	−3.041	2.153	24.81	—	—	1,2,3
4246	831	2.923	−2.494	1.526	24.82	167	5.3	2
4247	547	1.776	−1.775	0.036	24.90	88	4.3	2
4248	599	2.628	−2.564	0.577	24.89	136	4.7	2
4250	484	1.823	−1.771	−0.435	24.92	165	4.2	2
4252	703	1.757	−1.756	−0.037	24.89	180	1.8	3
4254	451	3.410	−2.807	1.935	24.95	137	4.2	2
4255	664	2.628	−2.614	0.274	24.97	218	7.2	2
4256	626	4.767	−4.766	−0.110	25.00	75	3.7	2
4257	544	3.656	−3.652	0.167	25.03	294	1.5	3
4259	657	2.979	−2.579	1.490	25.05	136	3.8	2
4260	591	2.238	−2.238	0.054	25.05	148	4.7	2
4261	689	3.686	−3.663	0.404	25.05	142	4.7	2
4263	577	4.056	−3.964	0.858	25.11	138	3.8	2
4265	818	3.816	−3.516	−1.482	25.14	69	5.0	2
4266	597	4.993	−4.803	−1.365	25.15	103	6.4	2
4267	540	2.913	−2.908	−0.184	25.13	249	2.3	3
4268	645	1.886	−1.883	−0.106	25.11	213	1.6	3
4269	348	2.667	−2.633	0.424	25.14	136	4.1	2
4270	387	2.548	−2.493	0.526	25.17	410	2.5	3
4271	590	1.950	−1.879	0.521	25.24	86	4.1	2
4274	708	4.929	−4.870	0.760	25.23	100	1.4	3
4275	490	6.081	−6.052	0.591	25.20	269	2.0	3
4277	502	4.427	−4.390	−0.571	25.24	164	6.2	2
4278	654	2.993	−2.863	0.874	25.21	102	3.9	2
4280	624	3.441	−3.440	0.079	25.26	—	—	3,3
4283	698	2.138	−1.975	0.818	25.28	278	2.9	3
4285	331	2.253	−2.242	−0.221	25.26	167	4.6	2
4290	464	4.111	−4.025	0.835	25.40	58	4.4	2
4292	732	3.629	−3.173	−1.763	25.40	122	7.4	2
4295	876	3.570	−3.499	0.704	25.39	140	5.3	2
42100	551	3.271	−3.241	−0.440	25.42	101	4.2	2
42108	557	4.047	−4.029	0.380	25.69	58	3.0	2
42112	378	3.168	−2.766	−1.545	25.73	83	12.0	2
4301	771	7.511	−7.467	−0.814	23.67	404	5.0	2
4302	667	7.301	−7.301	0.029	23.97	307	5.2	2
4303	512	6.096	−5.682	−2.206	24.02	253	5.3	2
4304	667	6.401	−6.139	−1.813	24.25	238	4.8	2
4305	413	9.264	−8.925	−2.486	24.25	226	3.9	2
4306	718	7.038	−6.686	−2.197	24.35	251	4.6	2
4307	599	9.721	−9.646	−1.205	24.35	549	2.3	3
4308	547	8.940	−8.659	−2.223	24.34	410	2.8	3
4309	667	8.245	−8.223	−0.592	24.39	183	2.2	3
4310	540	8.651	−7.844	−3.650	24.38	204	2.4	3
4311	546	7.862	−7.291	−2.940	24.38	446	3.2	3
4312	570	7.529	−7.492	−0.749	24.42	504	2.4	3
4313	716	7.298	−7.289	0.360	24.46	274	2.1	3
4314	653	8.930	−8.927	0.193	24.51	204	2.2	3

TABLE 5—*Continued*

ID	V	R	X	Y	m_{5007}	Counts	FWHM	Run	ID	V	R	X	Y	m_{5007}	Counts	FWHM	Run
4315	706	7.253	−6.790	−2.548	24.74	281	2.0	3	5106	506	9.685	9.052	−3.446	24.70	117	3.5	2
4316	772	9.671	−9.513	−1.740	24.76	232	1.5	3	5108	513	9.499	9.040	−2.916	24.86	113	4.1	2
4317	748	6.972	−6.951	−0.542	24.80	183	2.1	3	5110	428	9.088	7.786	−4.688	24.94	49	3.3	2
4318	797	7.360	−7.290	−1.014	25.08	172	5.5	2	5111	590	9.262	7.996	−4.675	25.03	230	4.5	2
4405	660	7.259	−0.588	7.235	23.87	—	—	3,3	5113	554	9.776	8.162	−5.380	25.18	112	4.2	2
4407	615	5.828	0.571	5.800	23.97	274	5.2	2	5114	296	9.672	8.459	−4.689	25.33	83	5.0	2
4409	591	4.137	0.377	4.120	24.23	226	5.2	2	5121	545	7.011	6.430	−2.796	26.08	49	2.9	2
4410	742	7.455	−0.223	7.452	24.19	727	2.4	3	5126	484	7.936	7.749	−1.715	26.65	44	2.8	2
4412	521	4.380	−0.496	4.352	24.48	166	5.0	2	5201	453	8.666	5.145	−6.973	23.61	335	3.8	2
4413	635	6.328	−0.261	6.323	24.55	209	4.8	2	5202	453	7.905	5.642	−5.538	23.65	321	5.2	2
4414	597	4.942	−1.403	4.738	24.51	135	4.6	2	5203	250	10.713	6.494	−8.520	24.03	142	4.3	2
4416	533	5.421	−1.704	5.146	24.62	181	5.0	2	5204	409	7.544	4.634	−5.952	24.52	115	4.1	2
4417	326	3.460	−0.737	3.381	24.59	—	—	1,2,3	5205	574	9.340	7.081	−6.090	24.93	117	4.4	2
4418	620	4.291	0.235	4.284	24.88	218	2.2	3	5206	402	8.365	6.753	−4.937	24.92	—	—	2,2
4419	700	4.989	0.024	4.989	24.82	182	5.1	2	5207	447	11.518	8.416	−7.865	24.96	116	3.4	2
4420	540	3.135	−0.889	3.006	24.88	239	1.8	3	5208	445	9.614	6.499	−7.084	25.08	128	6.8	2
4421	785	5.350	−1.873	5.011	24.85	319	2.3	3	5209	511	8.171	5.331	−6.193	25.33	144	7.6	2
4422	635	6.445	−1.635	6.234	25.01	91	4.3	2	5215	510	9.978	5.809	−8.113	26.13	45	2.8	2
4423	585	5.427	−1.566	5.196	25.00	251	2.4	3	5301	523	7.195	2.437	−6.769	23.85	253	4.7	2
4424	488	6.784	−0.220	6.781	25.12	493	2.3	3	5302	529	7.099	0.747	−7.059	24.31	—	—	2,3
4425	479	3.983	−1.147	3.814	24.94	54	4.2	2	5303	546	9.196	3.815	−8.368	24.35	186	4.1	2
4429	542	5.383	2.137	4.940	25.22	118	3.9	2	5305	465	6.407	1.569	−6.212	24.72	330	4.4	2
4433	610	7.271	0.458	7.257	25.67	59	4.4	2	5309	357	8.673	2.555	−8.288	25.03	121	4.3	2
4501	365	7.622	−6.385	4.162	24.09	363	4.5	2	5310	385	6.796	0.674	−6.763	25.06	165	4.4	2
4502	469	6.190	−4.497	4.254	24.13	281	4.6	2	5314	390	7.870	3.056	−7.253	25.49	101	5.0	2
4504	553	6.738	−4.976	4.542	24.28	242	4.2	2	5315	576	6.901	0.908	−6.841	25.47	74	4.3	2
4505	489	5.659	−3.512	4.436	24.32	234	4.9	2	5316	629	6.593	1.297	−6.464	25.71	61	4.3	2
4506	411	5.511	−4.188	3.582	24.32	164	7.1	2	5321	617	7.592	2.758	−7.073	26.59	42	3.3	2
4507	744	7.871	−6.305	4.711	24.33	271	4.5	2	5407	572	6.186	−2.643	−5.593	24.04	291	4.6	2
4508	564	6.664	−5.623	3.576	24.36	296	4.6	2	5408	383	4.763	−1.272	−4.590	24.11	188	5.4	2
4509	708	8.068	−5.600	5.808	24.37	282	4.6	2	5409	685	5.791	−1.920	−5.463	24.12	212	3.9	2
4510	469	5.903	−4.754	3.499	24.41	224	4.6	2	5410	690	4.985	−0.804	−4.919	24.21	255	4.5	2
4511	687	6.255	−5.636	2.715	24.49	267	4.4	2	5413	420	5.062	−1.214	−4.914	24.24	386	5.3	2
4512	767	7.862	−6.757	4.018	24.52	385	2.1	3	5415	574	5.452	−2.043	−5.055	24.28	202	4.3	2
4514	448	7.807	−6.710	3.991	24.67	330	2.5	3	5416	449	6.203	−1.596	−5.994	24.26	205	4.9	2
4515	456	7.738	−4.886	6.000	24.68	234	5.2	2	5417	286	3.555	−1.452	−3.245	24.30	198	5.0	2
4516	328	5.714	−4.537	3.473	24.67	244	1.8	3	5418	425	5.529	−1.284	−5.378	24.32	192	5.4	2
4517	506	7.391	−6.791	2.916	24.76	215	4.5	2	5419	396	3.762	−1.126	−3.589	24.51	323	4.3	2
4518	491	7.294	−6.073	4.039	24.77	387	2.3	3	5420	515	2.781	−0.879	−2.639	24.57	144	1.5	3
4519	439	9.914	−8.548	5.023	24.86	172	4.2	2	5421	566	4.389	−1.174	−4.229	24.60	286	4.6	2
4521	732	6.576	−4.422	4.867	24.93	127	4.4	2	5422	312	3.122	−1.095	−2.924	24.66	246	4.6	2
4522	588	6.832	−5.187	4.446	25.08	493	3.8	3	5423	511	2.781	−0.879	−2.639	24.60	326	2.0	3
4523	816	5.887	−4.564	3.718	25.08	322	1.7	3	5424	575	5.122	0.741	−5.068	24.61	239	4.4	2
4525	375	7.414	−6.830	2.885	25.13	457	3.8	3	5425	559	6.974	−2.024	−6.674	24.64	121	4.0	2
4603	661	6.844	3.005	6.149	24.17	306	2.7	3	5427	550	4.205	−0.080	−4.204	24.73	170	4.1	2
4604	643	7.581	1.529	7.425	24.33	—	—	3,3	5428	560	3.464	−0.643	−3.404	24.74	180	4.6	2
4606	463	8.718	4.308	7.580	24.42	182	2.2	3	5429	529	3.972	−0.041	−3.972	24.87	80	4.5	2
4607	481	9.013	4.428	7.850	24.61	222	1.4	3	5430	456	3.785	−0.673	−3.725	24.92	89	5.9	2
4608	597	10.814	2.805	10.444	24.57	335	2.4	3	5431	488	5.716	1.635	−5.477	24.92	143	5.5	2
4609	481	7.440	0.797	7.397	24.75	561	3.8	3	5432	704	4.596	−0.128	−4.594	24.92	119	5.6	2
4610	459	9.512	2.783	9.096	25.08	351	2.5	3	5436	386	6.549	−0.550	−6.526	25.04	158	4.1	2
4701	393	8.933	−1.279	8.841	24.08	320	1.8	3	5438	473	5.472	−1.258	−5.326	25.11	93	4.3	2
4702	472	11.475	−1.448	11.383	24.87	—	—	3,3	5440	376	6.880	−0.483	−6.863	25.18	63	4.2	2
4801	578	10.799	−5.506	9.289	23.78	420	2.2	3	5441	650	5.651	−0.154	−5.649	25.14	215	4.6	2
4802	605	9.598	−3.020	9.110	24.42	389	2.5	3	5442	353	5.314	1.407	−5.124	25.44	102	5.2	2
4803	369	8.962	−3.489	8.254	24.44	546	3.4	3	5444	618	4.493	0.630	−4.448	25.47	64	3.8	2
4804	712	9.414	−5.053	7.943	24.74	258	2.3	3	5445	677	3.462	−1.217	−3.241	25.49	239	3.8	3
4805	517	12.176	−5.636	10.793	24.70	731	2.6	3	5446	431	4.628	0.955	−4.529	25.63	58	5.1	2
4806	680	10.062	−5.795	8.226	24.78	234	1.6	3	5461	666	4.729	−2.436	−4.053	26.07	43	4.5	2
4807	702	12.127	−5.019	11.040	24.76	418	3.6	3	5466	448	4.567	−0.458	−4.544	26.29	76	5.4	2
4808	503	9.396	−4.289	8.360	25.47	259	2.4	3	5501	572	8.461	−1.001	−8.401	24.15	407	4.1	2
5101	658	7.814	6.562	−4.243	23.87	348	5.0	2	5502	578	8.985	−0.733	−8.955	24.50	224	4.1	2
5102	551	9.353	8.510	−3.879	24.22	—	—	2,3	5503	389	7.930	−0.971	−7.871	24.70	—	—	2,2
5103	344	7.849	6.800	−3.921	24.25	217	4.4	2	5504	333	7.840	−0.889	−7.789	24.82	100	1.4	3
5104	542	8.018	7.683	−2.291	24.48	182	4.5	2	5504	371	7.840	−0.889	−7.789	24.82	155	4.1	2
5105	241	8.949	8.425	−3.017	24.67	153	5.1	2	5505	509	9.261	0.172	−9.259	24.81	—	—	2,2

TABLE 5—*Continued*

ID	V	R	X	Y	m_{5007}	Counts	FWHM	Run	ID	V	R	X	Y	m_{5007}	Counts	FWHM	Run
5506	459	10.661	−2.590	−10.342	25.00	104	4.9	2	5617	742	9.788	−6.028	−7.712	25.58	70	5.7	2
5508	439	10.021	0.078	−10.021	25.67	110	5.1	2	5619	575	7.918	−2.122	−7.628	25.70	—	—	2,2
5510	333	8.893	−0.480	−8.880	25.80	47	3.7	2	5620	559	7.716	−4.093	−6.541	25.77	47	3.3	2
5511	554	9.686	−1.095	−9.624	25.81	54	3.7	2	5621	589	8.907	−3.441	−8.216	25.64	51	4.9	2
5514	562	11.069	−2.245	−10.839	25.93	47	3.3	2	5622	566	8.986	−4.592	−7.724	25.80	59	6.2	2
5601	272	9.123	−3.707	−8.337	23.51	190	4.3	2	6101	547	9.088	−8.069	−4.182	23.85	136	4.2	2
5602	308	7.482	−2.778	−6.947	24.17	309	4.7	2	6102	658	9.629	−8.159	−5.115	24.15	250	5.0	2
5603	531	9.337	−5.696	−7.399	24.45	225	4.1	2	6103	629	8.187	−7.029	−4.197	24.00	120	4.2	2
5604	513	7.020	−3.282	−6.206	24.67	205	5.5	2	6104	218	6.243	−3.812	−4.945	24.10	174	4.9	2
5605	417	10.072	−4.535	−8.993	24.79	143	3.8	2	6105	588	7.929	−6.296	−4.819	24.33	187	4.2	2
5606	668	10.520	−3.742	−9.832	24.77	80	4.6	2	6106	532	9.150	−7.144	−5.718	24.42	103	4.1	2
5607	277	10.238	−5.804	−8.434	24.78	70	4.4	2	6107	513	9.488	−6.020	−7.334	24.68	288	2.1	3
5608	466	7.977	−2.872	−7.442	24.88	129	4.5	2	6108	350	6.840	−5.560	−3.985	24.61	—	—	2,3
5609	419	8.188	−2.745	−7.714	24.85	356	3.8	3	6110	280	6.668	−4.485	−4.934	24.86	79	4.5	2
5610	385	10.202	−4.357	−9.224	24.86	87	4.4	2	6111	655	8.861	−6.907	−5.551	24.74	—	—	3,3
5611	545	8.411	−2.737	−7.953	24.99	102	5.8	2	6113	524	7.223	−5.328	−4.876	24.98	127	4.1	2
5612	385	9.340	−5.519	−7.536	25.07	110	5.1	2	6116	571	7.302	−5.888	−4.318	25.33	71	5.7	2
5615	571	9.618	−3.943	−8.773	25.13	25	3.1	2	6117	638	6.837	−6.137	−3.013	25.38	98	4.7	2
5616	446	9.731	−4.990	−8.354	25.36	116	4.7	2									

5.2. *Planetary Nebula as Dynamical Test Particles of the Elliptical Component*

The observed PN population belongs to the elliptical component of the galaxy as the PN spatial distribution follows that of the light (Paper I). Nevertheless, the dust lane of the galaxy has distinctively different kinematics from the elliptical component. To make sure that our velocities are not contaminated by disk objects, the kinematics and spatial distribution of the PN candidates were compared with those of the H II regions of the disk (Graham 1979). As a result, we reclassified 17 PN candidates as disk objects. A strong Hβ line in the spectra of these objects confirms their nature as H II regions.

After the above procedure, the disk contamination in the PN sample is minimal. Figure 8*a* plots velocities of the H II regions against the azimuthal angle Θ in the plane of the disk for both the Graham sample (*solid triangles*) and our sample (*stars*). In calculating Θ, we assume that the disk inclination is 73°, and the line of nodes is along the photometric minor axis at P.A. = 125° (Graham 1979). As shown in the figure, the velocities follow a sinusoid curve as expected for a rotating disk. At the same time, the H II regions form a ring structure on the sky (Fig. 8*b*). Also plotted in the two figures are PNs that happen to fall close to the disk rotation curve. Their spatial distribution is totally random with respect to the ring defined by the H II regions. Therefore, these PNs are not kinematically related to the dust lane. Similar to Figure 8*a*, Figure 9 plots velocities of all PNs against Θ. It is obvious that the PNs do not follow the H II regions kinematically.

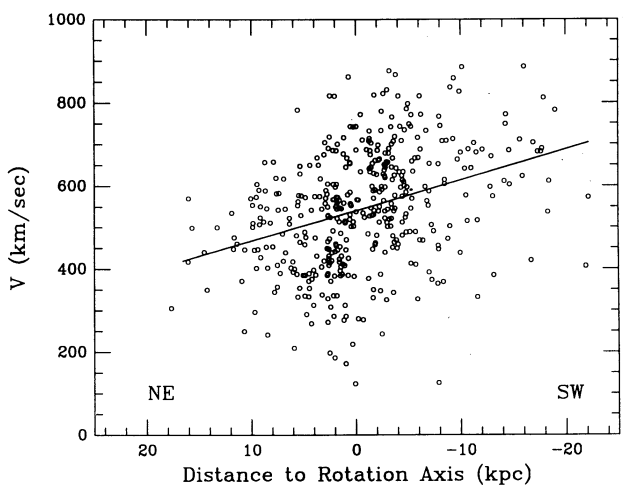

FIG. 7.—Radial velocity vs. distance to the rotation axis for all PN velocities. The straight line is a linear fit to the data.

5.3. *A Schematic Planetary Nebula Velocity Field*

The PN velocities cover the entire galaxy to a radius of ~10 kpc[8] and extend along the photometric major axis out to ~20 kpc. Their spatial distribution is shown in Figure 10, where the symbols correlate with the velocities: a circle is used if the nebula is approaching, and a cross is used if it is receding; the size of the symbol is such that higher velocities correspond to larger symbols. To reduce the scatter of the intrinsic velocity dispersion, each nebular velocity is replaced by the mean velocity of its neighboring PNs within 1.5 kpc radius. Therefore, the figure is in fact a representation of the mean PN velocity field. Also shown in the figure are the approximate isophotes of the galaxy (D79). The semimajor axes of the ellipses vary from 1 to $4r_e$ with a step size of $1r_e$ (~5.18 kpc; D79).

We will discuss the details of the PN velocity field in the subsections to follow, but a few things are worth mentioning here. First, the nebulae apparently rotate around both the photometric major and minor axes. The line of zero rotation (the rotation axis) lies somewhere in between. Second, the PN velocities extend to as far as $4r_e$, a factor of 4 increase in radius compared to the observations of elliptical galaxies made in integrated light. Finally, there are virtually no PNs found in the central 3 × 6 kpc region owing to the obscuration of the dust lane. Other blank areas in the distribution are due to

[8] We adopt 3.5 Mpc as the distance to NGC 5128 (Paper I). All quantities in this paper, including those taken from references, are scaled to this distance. The corresponding scale is 1′ = 1.02 kpc.

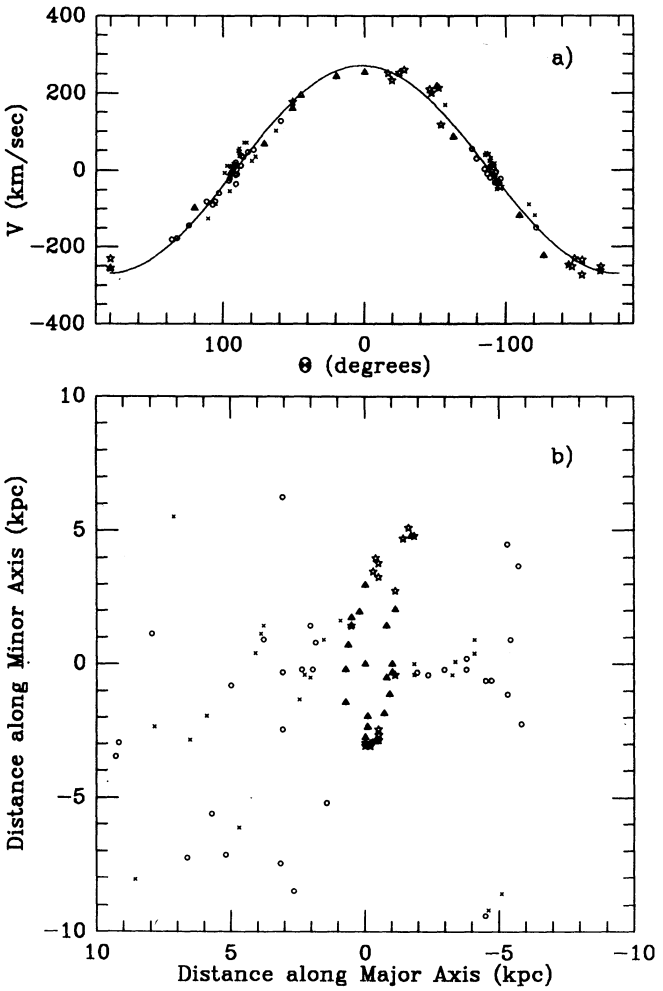

FIG. 8.—(*a*) Velocity vs. position angle. The systemic velocity is subtracted from V. The angle Θ is defined in the plane of the disk ($\Theta = 0°$ at P.A. = 305°). (*b*) Spatial distribution of the objects in (*a*). Coding of the symbols: (*solid triangles*) H II regions in Graham (1979); (*stars*) H II regions in our sample; (*circles*) PNs whose velocities are within 20 km s^{-1} of the disk rotation curve; (*crosses*) PNs with velocities differing by 20 to 40 km s^{-1} from the disk rotation.

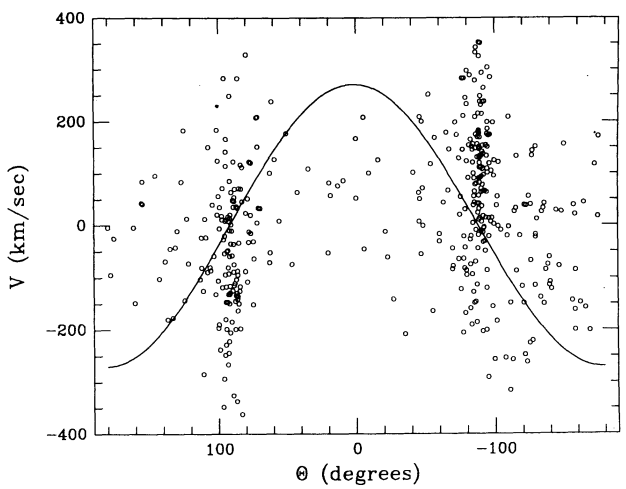

FIG. 9.—Velocity vs. position angle for all PNs. The sinusoid curve defines the rotation of the disk. It is obvious that the PNs have different kinematics from that of the H II regions.

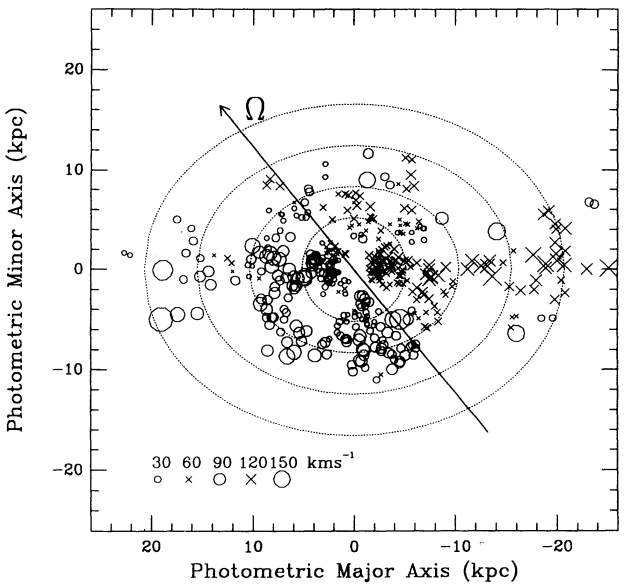

FIG. 10.—The PN spatial distribution. The symbol representing each nebula is chosen so that circles are for velocities approaching and crosses for receding (see text). The legend in the lower left relates the sizes of the symbols to the velocities. The ellipses are the appropriate isophotes, and the letter Ω marks the position of the rotation axis.

the incomplete spatial coverage of our survey (see Fig. 1 of Paper I).

5.4. *Rotation Axis*

Given the two dimensional PN velocity field, the rotation axis on the sky can be readily obtained by examining the velocity variation as a function of azimuthal angle. We fit a function

$$V = A \times \sin(\Phi - \Phi_0) + V_0 \quad (1)$$

to the individual PN velocities in a ring between 5 and 10 kpc radius where the PN spatial coverage is the most complete (Fig. 10). In the equation, Φ is the azimuthal angle on the sky with respect to the photometric minor axis at P.A. = 305° and is positive eastward. A simple wave function is chosen because any higher order terms are not justified given the scatter in the data. The best fit yields $\Phi_0 = 39° \pm 10°$. It implies that the rotation axis is at P.A. = 344° ± 10°, a significant misalignment of 39° from the minor axis. The azimuthal variation of the rotation velocities is shown in Figure 11*a* along with the best-fitting function. The plotted velocities are the mean of 10

TABLE 6

ROTATION VELOCITY VERSUS POSITION ANGLE

Φ	V (km s^{-1})	Φ	V (km s^{-1})
170° ± 5°	487 ± 30	−39° ± 9°	540 ± 42
147 ± 10	486 ± 22	−55 ± 3	525 ± 49
121 ± 5	494 ± 38	−77 ± 11	591 ± 38
106 ± 3	445 ± 39	−97 ± 4	664 ± 33
92 ± 5	471 ± 51	−111 ± 4	588 ± 30
74 ± 7	486 ± 23	−129 ± 6	530 ± 40
45 ± 6	528 ± 11	−148 ± 5	481 ± 49
15 ± 11	565 ± 29	−160 ± 3	529 ± 33
−11 ± 8	606 ± 37	−172 ± 4	451 ± 27

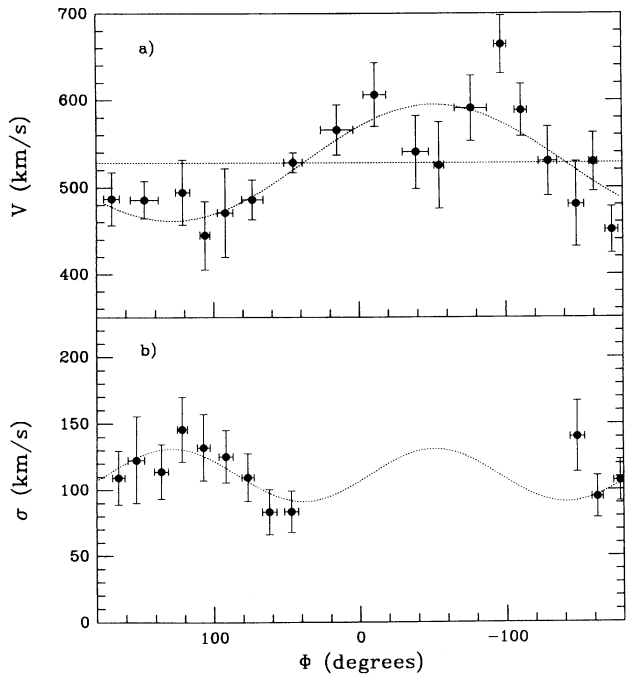

FIG. 11.—(*a*) Rotation velocity vs. position angle on the sky for PNs between 5′ and 10′. The PNs are binned in groups of 10. The angle Φ is zero at the minor axis P.A. = 305° and increases eastward. The dotted curve is the best-fitting function to individual PN velocities. The misalignment between the photometric minor axis and the rotation axis is 39°. (*b*) Azimuthal modulation of the PN velocity dispersion. PNs with $x < 0$ are folded onto the other half of the galaxy. The dotted curve is the best-fitting function.

PNs in each bin. The numerical values are given in Table 6. The rotation axis is also marked on Figure 10 with the letter Ω.

The large offset between the photometric and dynamical axes provides convincing evidence that NGC 5128 is not an axisymmetric system. Otherwise, the rotation axis would be along either the photometric minor axis (oblate spheroid) or major axis (prolate spheroid). Instead, the galaxy may be triaxial, in which case the observed rotation axis may coincide with neither photometric axis. Two effects can contribute to the misalignment. Generically, stars can rotate around both the intrinsic short axis and long axis in a triaxial potential (see Statler 1987). The net angular momentum vector could be anywhere in the plane defined by these two axes. Furthermore, for a triaxial ellipsoid the observed photometric axes are generally not the principal axes in projection; thus, the projection effect could also introduce the misalignment even if the short axis is intrinsically the rotation axis (Stark 1977; Binney 1985). Given the observed misalignment, we will assume that NGC 5128 is triaxial in the subsections to follow.

Rotation axis twist may be expected when observing a triaxial system from certain viewing angles (Statler 1991a). We divide the PN sample into three annuli to check this possibility. When equation (1) is applied by keeping V_0 to be the systematic velocity of 541 km s^{-1}, statistically acceptable fits are obtained for all three groups (Table 7). The results suggest that the position angles of the rotation axis at different radii are consistent with P.A. = 344° ± 10°. Because the PN spatial distribution is not uniform, we can only tentatively conclude that no significant rotation axis twist is present in the radius range of 1.5 to 12 kpc.

TABLE 7

POSITION ANGLE OF THE ROTATION AXIS AT DIFFERENT RADII

Range (kpc)	χ^2	Numbers of PNs	P.A.
1.5–4.....	136	133	345° ± 20°
4–8.....	162	151	343 ± 11
8–12.....	102	96	341 ± 11

5.5. *Azimuthal Velocity Dispersion Modulation*

To examine an azimuthal modulation in velocity dispersion, we take advantage of a point-reflecting symmetry about the galactic center to improve the sampling. Such symmetry is warranted so long as the galaxy is in equilibrium. In a coordinate system where the x-axis is perpendicular to the rotation axis, we reflect those PNs with $x < 0$ onto the other half of the galaxy following: $x = -x$, $y = -y$, and $v = -v$, where velocity v is relative to the galactic center. The PNs between 5 and 10 kpc are grouped in intervals of 15°. The rms velocity scattering of each bin yields a velocity dispersion σ and its standard deviation $\sigma/(2n)^{1/2}$. The results are given in Table 8 and shown in Figure 11*b*. We fit a sinusoid curve of period π,

$$\sigma = \sigma_1 \sin [2(\Phi - \Phi_1)] + \sigma_0 , \quad (2)$$

to the dispersion variation. Here Φ is the same as in equation (1). The best parameters are: $\sigma_1 = 20 \pm 8$, $\Phi_1 = 84.^{\circ}5 \pm 23^{\circ}$ and $\sigma_0 = 111 \pm 6$ (shown on Fig. 11*b*).

The azimuthal variation of velocity dispersion is correlated with rotation in the sense that dispersion reaches its peak where the largest rotation is observed and drops to a minimum where the rotation is equal to zero. At approximately 7.5 kpc, the amplitude of the dispersion modulation is ~20 km s^{-1}, whereas the mean dispersion is ~110 km s^{-1}. This correlation suggests that the projection of the rotation along the line of sight contributes to the observed dispersion modulation. It may further imply that figure rotation is not important since it does not contribute to the line-of-sight velocity dispersion given the nature of its solid body rotation.

5.6. *Major and Minor Axis Velocity Profiles*

Figure 12*a* shows the PN velocity plotted against the distance along the photometric major axis. Since the minor axis is not a symmetric axis of the velocity field, only those PNs projected within 2′ of the major axis are included. The clustering of the velocities in the two diametrically opposed quadrants is an

TABLE 8

VELOCITY DISPERSON VERSUS POSITION ANGLE

Φ	σ	Number of PNs
−148 ± 5.....	140 ± 27	14
−162 ± 4.....	95 ± 16	17
−178 ± 4.....	107 ± 16	23
165 ± 4.....	109 ± 21	14
153 ± 6.....	123 ± 33	7
136 ± 5.....	114 ± 21	15
122 ± 4.....	145 ± 24	18
107 ± 4.....	132 ± 25	14
92 ± 5.....	125 ± 20	20
77 ± 4.....	109 ± 18	18
62 ± 5.....	83 ± 17	12
47 ± 5.....	83 ± 16	14

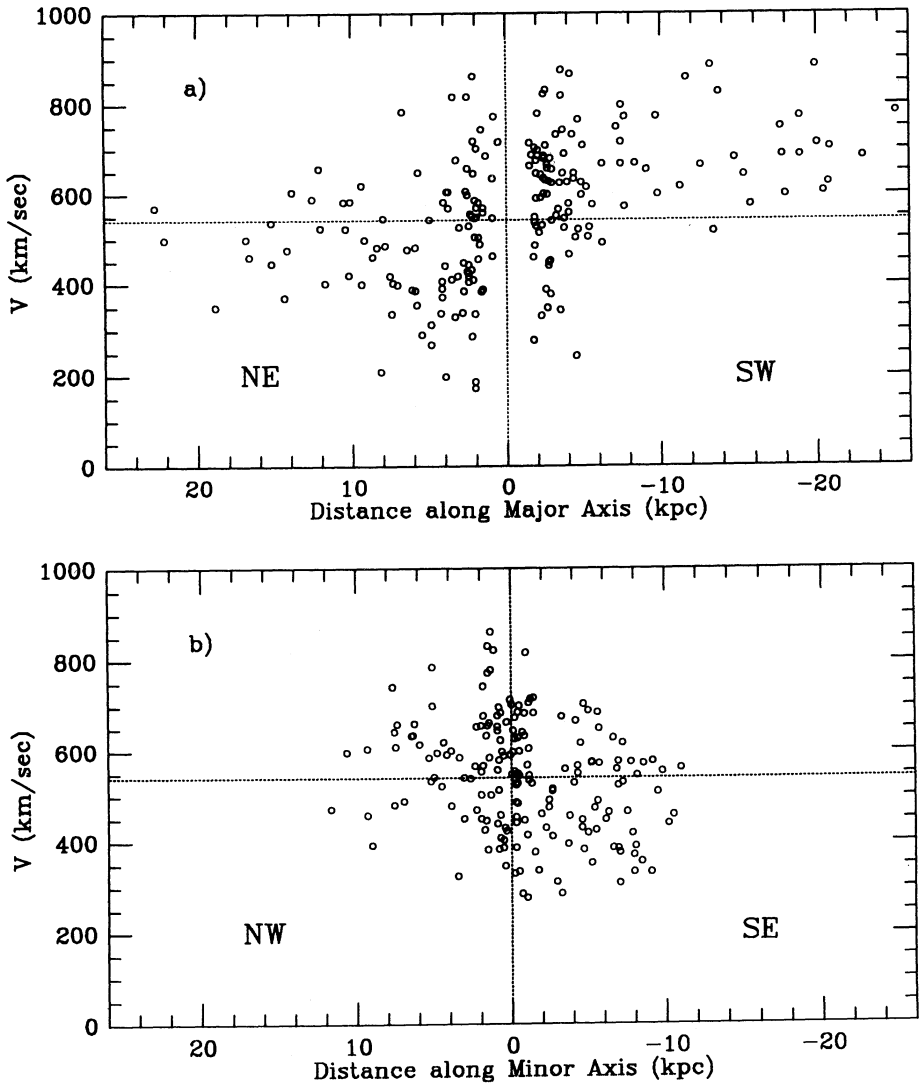

FIG. 12.—(*a*) PN radial velocity vs. distance along the photometric major axis. Only those PNs within 2′ of the major axis are plotted. (*b*) Velocities of PNs within 3′ of the minor axis against the distance along the photometric minor axis. The horizontal line in each panel marks the systematic velocity of 541 km s^{-1}.

unmistakable signature of major axis rotation (northeast approaching, southwest receding). Similarly, the minor axis rotation is also significant, as seen in Figure 12*b*, where only PNs within 3′ of the minor axis are plotted. The minor axis rotation is in the same direction as the dust lane (southeast approaching, northwest receding).

We construct the major and minor rotation curves and velocity dispersion profiles based on the data in Figure 12. For the major axis, the PNs in the northeast are folded onto the southwest side. The PNs are binned in 2′ intervals inside 10′ and in 5′ intervals at larger radii. The mean velocity and its standard deviation yield a rotation velocity and a velocity dispersion for each bin. Similarly, the minor axis rotation curve and velocity dispersion profile are obtained by reflecting the southeast side PNs onto the northwest. The PNs are grouped in 2.5 intervals. The numerical values of the rotation and velocity dispersion are listed in Table 9 and plotted in Figure 13.

Along the major axis, the rotation increases with radius in the inner galaxy and reaches approximately 100 km s^{-1} at about 7 kpc. Beyond that, the rotation is nearly flat. The veloc-

TABLE 9

MAJOR AND MINOR AXIS VELOCITY PROFILES

Number of PNs	R (kpc)	V (km s^{-1})	σ (km s^{-1})	V/σ
		Major Axis		
31	1.6 ± 0.4	−2 ± 22	123 ± 16	−0.02 ± 0.18
80	2.7 ± 0.6	48 ± 16	143 ± 11	0.34 ± 0.14
31	4.7 ± 0.6	83 ± 25	131 ± 17	0.63 ± 0.26
17	7.0 ± 0.6	102 ± 29	121 ± 21	0.84 ± 0.39
11	8.9 ± 0.6	97 ± 35	115 ± 24	0.84 ± 0.48
19	12.5 ± 1.6	85 ± 30	129 ± 21	0.66 ± 0.34
12	17.5 ± 1.5	146 ± 26	91 ± 18	1.60 ± 0.62
7	21.7 ± 1.6	100 ± 33	88 ± 24	1.14 ± 0.68
		Minor Axis		
94	1.0 ± 0.6	22 ± 13	130 ± 10	0.17 ± 0.12
32	3.8 ± 0.7	19 ± 20	111 ± 14	0.17 ± 0.20
35	6.2 ± 0.8	53 ± 16	97 ± 12	0.54 ± 0.23
16	8.4 ± 0.7	62 ± 29	117 ± 21	0.53 ± 0.34
5	10.6 ± 0.5	30 ± 32	72 ± 23	0.42 ± 0.58

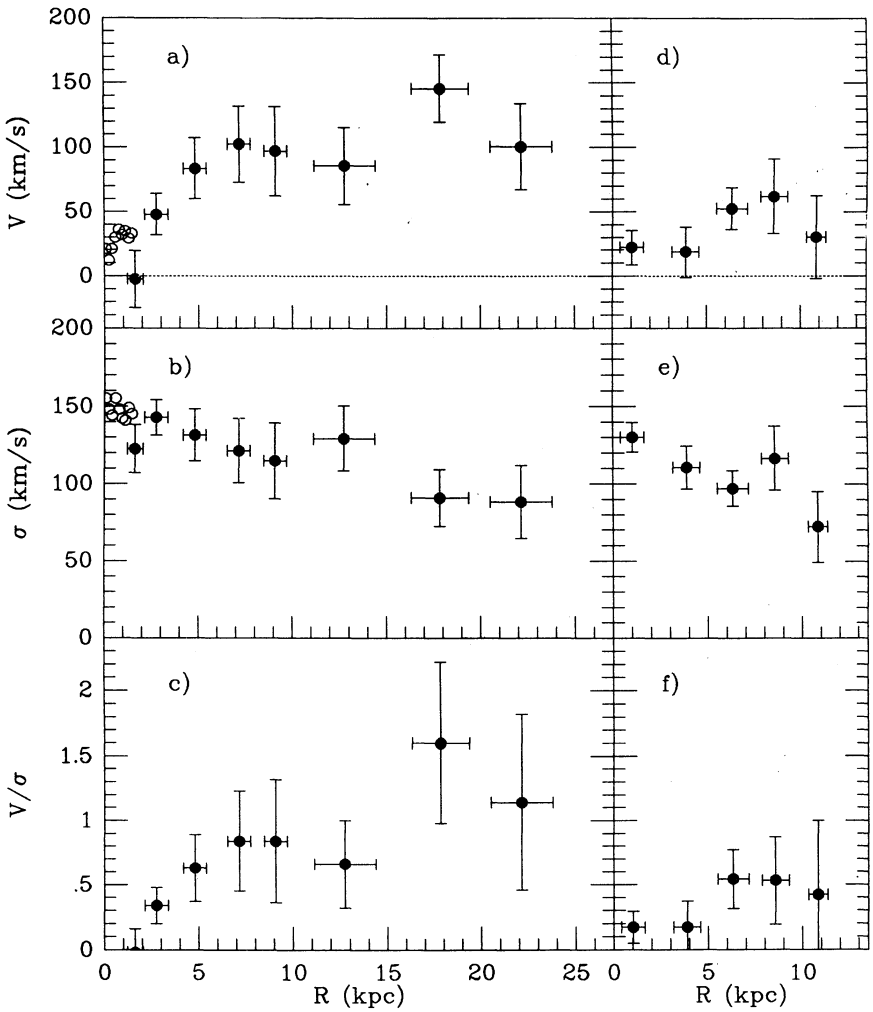

FIG. 13.—(*a*) PN major axis rotation curve (*filled circles*). The empty circles are the long-slit data from WSFW (see text). (*b*) PN major axis velocity dispersion profile. (*c*) Local V/σ ratio along the major axis; (*d*), (*e*) and (*f*) are the same, but for the minor axis. Given $1r_e = 5.18$ kpc (D79), the major axis rotation curve and velocity dispersion profile extend to approximately $4r_e$.

ity dispersion is about 143 km s^{-1} at 2.8 kpc and then declines slowly throughout the halo to ~90 km s^{-1} at 20 kpc. The streaming motion becomes more important with increasing radius. The local V/σ ratio is about 1 outside 10 kpc (Fig. 13*c*). The minor axis rotation is about 50 km s^{-1} between 5 and 10 kpc. By comparing with the velocity dispersion, we find that the V/σ ratio is about 0.5 for the minor axis rotation (Fig. 13*f*).

WSFW studied the dynamics of NGC 5128 through absorption spectra. They observed the photometric major axis using the long slit which extended to 400″ on the northeast side and 84″ on the southwest. For comparison, the major axis rotation and velocity dispersion of the long-slit spectra (their Table 2) in the inner 90″ are averaged in 10″ intervals and overplotted in Figures 13*a* and 13*b*. The PN velocities agree with the long-slit observation in the trend (the innermost PN points on both figures are probably not significant). Beyond 90″, both the rotation and velocity dispersion of the slit spectra decrease rapidly and are in poor agreement with the PN data. WSFW cautioned that the velocities at radii larger than 90″ suffer greater uncertainties since no velocity template was taken for the slit used in the region. High signal-to-noise ratio spectra are needed before a meaningful comparison can be made at large radii.

A velocity map of the central 185″ × 134″ region was also obtained by WSFW using the RGO spectrograph in a scan mode on the AAT. Although no significant minor axis rotation is seen in the map, they reported that there might be an offset of 10° between the photometric minor axis and the line of zero velocity. This offset is smaller than the PN rotation axis offset of 39° but is in the same direction. This could be understood as the skew of the line of zero rotation, which is not unusual for triaxial galaxies (Statler 1991a). Given the quality of the velocity map, we believe that confirmation of this effect awaits a spatially more extended, higher signal-to-noise ratio velocity mapping.

5.7. *Line of Maximum Rotation Amplitude*

Because of the large intrinsic velocity dispersion and the spatial incompleteness of our sample, it is difficult to make a velocity contour map out of the PN data. Instead, we group the PNs within 10 kpc radius into 2′ × 2′ grids and construct a two-dimensional PN velocity map using the mean velocity at

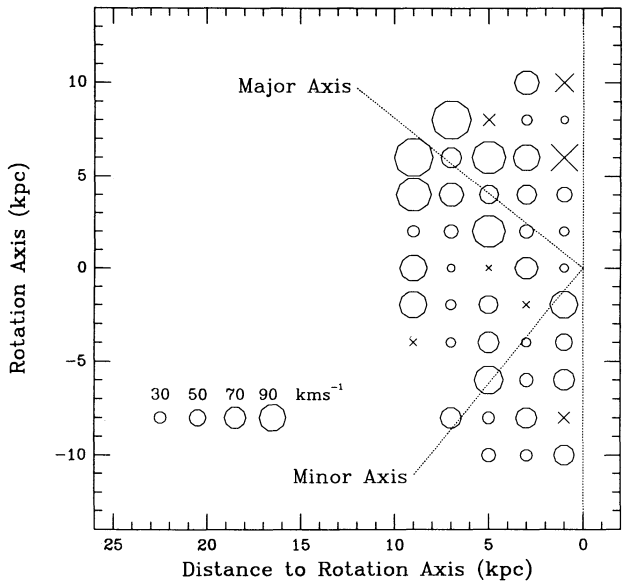

FIG. 14*a*

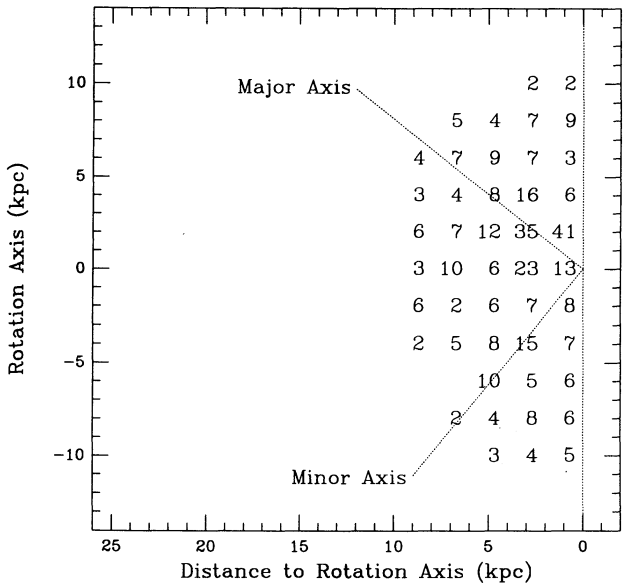

FIG. 14*b*

FIG. 14.—(*a*) PN velocity field. The PNs are grouped into 2′ × 2′ grids. The mean velocity of each grid is plotted in the figure. The circles are for velocities approaching, and the crosses for receding. The symbol sizes are related to the velocities as explained by the legend in the lower left. (*b*) Number of PNs in each grid, which gives a sense of statistical significance of each velocity in (*a*).

each point. The PN velocities are folded onto one half of the galaxy following the method described in § 5.5. The velocity map is shown in Figure 14*a* with its abscissa in the direction perpendicular to the rotation axis and its ordinate along the rotation axis. In a similar fashion to Figure 10, different symbols and sizes are used to represent the velocities. The number of PNs in each grid is shown in Figure 14*b*. On both figures, the positions of the photometric axes are also marked. By examining Figure 14*a* we conclude that the maximum rotation is likely along the photometric axis. Consequently, the line of zero rotation is not perpendicular to the line of maximum rotation. A similar velocity field is seen in NGC 4589 (Möllenhoff & Bender 1989). The phenomena can be understood within the context of triaxial galaxies (Binney 1985; Levison & Richstone 1987; Statler 1991a) where the projected rotation axis and the line of maximum velocity amplitude are typically not orthogonal.

5.8. *Comparison with the Globular Cluster System*

Because of its proximity, the kinematics of the NGC 5128 globular cluster system is the best studied beyond the local group. Using the velocities of ~80 clusters (Harris, Harris, & Hesser 1988; Sharples 1988), Harris et al. (1988) showed marginal evidence for cluster rotation around both the photometric minor and major axis. The reported rotation is in the same sense as that of the PNs, but the amplitude of the cluster rotation is much smaller (Fig. 5, Harris et al. 1988).

More recently, the metallicities of 62 clusters were derived by Harris et al. (1992) through the integrated photometry of the Washington System. Using the published metallicities and velocities, we are able to divide the clusters into metal-rich and metal-poor groups with a somewhat arbitrary dividing point, [Fe/H] = −1.0. The cluster rotations around both major and minor axes for the two groups are shown in Figure 15. The figure suggests that while the metal-poor clusters lack any significant rotation, the metal-rich ones do rotate in the same sense as the PNs. Furthermore, the major and minor axis rotations are both about 40 km s^{-1} inside of 6 kpc, consistent with the amplitude of the PN rotation (Fig. 13).

6. MASS DISTRIBUTION

The study of galactic mass distribution depends on knowledge of the orbital structure of stars. Because elliptical galaxies as a class are triaxial (Illingworth 1977; Binney 1978), their intrinsic shapes and stellar orbits have a wide range, and thus the deprojection of the line-of-sight velocity is not unique. To derive the mass distribution, certain assumptions about velocity anisotropy have to be made. An exception is found in elliptical galaxies harboring extended cold gas, such as NGC 5128. Assuming that the gas is in equilibrium with the stellar body, its kinematics provides strong constraint on the galactic mass distribution. In this case, important information about the stellar orbits can also be obtained.

The rotation curve of NGC 5128's central disk were measured through the Hα emission (BTA; Nicholson, Bland-Hawthorn, & Taylor 1991, hereafter NBT), the neutral hydrogen 21 cm emission (van Gorkom et al. 1990) and the CO (2–1) emission (Quillen et al. 1992). Recently, Schiminovich et al. (1994) also detected an inclined H I ring at 15 kpc from the center of the galaxy with a rotation velocity of 250 km s^{-1}. The complete stellar rotation curve and velocity dispersion profile can be obtained by combining the PN data of 2 to 20 kpc with the stellar velocities in the inner 1.5 kpc measured from absorption spectra (WSFW; see also § 5.6). Because PNs are the post-AGB stars, the velocities measured from both PN and absorption spectra sample the same stellar velocity field. The two data sets define the rotation and velocity dispersion from the very center of the galaxy to the outer halo (Fig. 13).

In this section we will show that the central mass-to-light ratio derived using the stellar velocity dispersion in the inner 1.5 kpc is consistent with the constraint provided by the gas rotation, and the stellar orbits are most likely isotropic in the center. At large radii, we will apply the isotropic Jeans equation to the PN major axis velocity profiles to derive a mass-to-

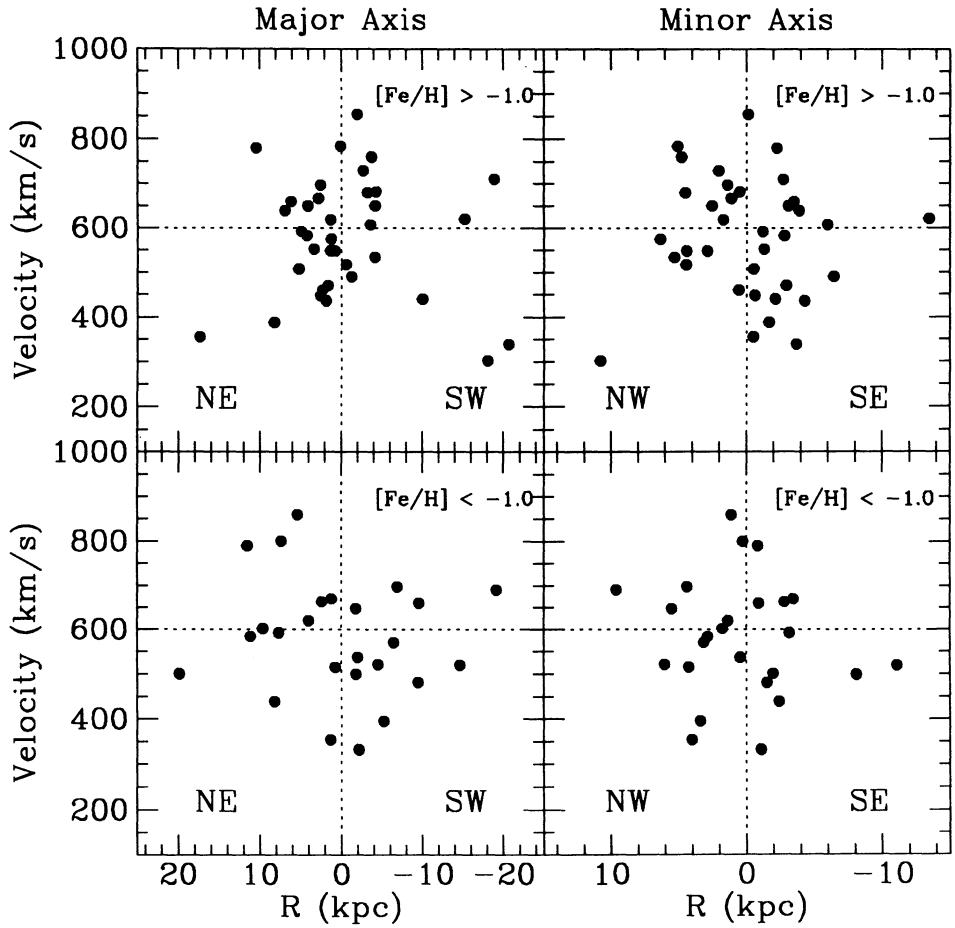

FIG. 15.—Globular cluster rotations around both photometric major and minor axes are shown. While the metal-poor group seems to have little rotation, the metal-rich clusters rotate as fast as the PNs. The horizontal line in each panel marks the systemic velocity derived with the globular cluster velocities.

light ratio which increases in the halo. Experimentation with an anisotropic model shows that the dark halo is indeed necessary. The kinematics of the 15 kpc H I ring and globular clusters (Harris et al. 1988; Sharples 1988) provides further checks on the mass distribution in the halo.

6.1. *Model*

Under spherical symmetry, the Jeans equation which relates global properties of a stellar system is given by

$$\frac{d(\rho\overline{v_r^2})}{dr} + \frac{\rho}{r}(2\overline{v_r^2} - \overline{v_\vartheta^2} - \overline{v_\varphi^2}) = -\frac{GM(r)\rho}{r^2}, \quad (3)$$

where $\rho = \rho(r)$ is the mass density of test particles, $M(r)$ is the total mass within radius r, and $\overline{v_r^2}$, $\overline{v_\vartheta^2}$, and $\overline{v_\varphi^2}$ are the second velocity moments.

We will apply the above Jeans equation to the major axis rotation and velocity dispersion to derive the mass distribution of the galaxy. In the application, the velocity dispersion is assumed to be isotropic. We will try to justify the assumption in the studies to follow. However, if the velocity dispersion becomes more tangential with increasing radius, the isotropic model overestimates the halo mass; on the other hand, the mass is underestimated if stellar orbits become more radial. We further assume that the streaming motion is around the z-axis only, so that

$$\overline{v_r^2} = \sigma^2, \quad \overline{v_\vartheta^2} = \sigma^2, \quad \overline{v_\varphi^2} = \sigma^2 + V_{\rm rot}^2, \quad (4)$$

where $\sigma^2(r)$ is the velocity dispersion, and $V_{\rm rot}(r)$ is the rotation velocity. Thus, equation (3) is reduced to

$$\frac{d(\rho\sigma^2)}{dr} = -\frac{GM(r)\rho}{r^2} + \frac{\rho V_{\rm rot}^2}{r}, \quad (5)$$

which can be solved for the velocity dispersion

$$\sigma^2 = \rho^{-1}\int_r^\infty \frac{GM(x)\rho}{x^2}dx - \rho^{-1}\int_r^\infty \frac{\rho V_{\rm rot}^2}{x}dx. \quad (6)$$

To obtain a solution for σ, we have to make assumptions about the mass density ρ, the mass distribution $M(x)$, and the rotation $V_{\rm rot}$. D79 obtained high-quality surface photometry of NGC 5128 inside 8′. They found that the galaxy's light distribution follows a de Vaucouleurs law. Therefore, we adopt the Hernquist mass model, which closely resembles the de Vaucouleurs law, for the distribution of the luminous matter (Hernquist 1990). The model allows dynamical properties of a galaxy to be evaluated analytically (de Zeeuw 1990). The spatial mass density of the model is

$$\rho(r) = \frac{M_l a}{2\pi}\frac{1}{r(r+a)^3}, \quad (7)$$

where the scale length $a = r_e/1.8153$, with r_e being the effective radius of the de Vaucouleurs law. The corresponding gravitational potential has a finite total mass M_l.

We write the model mass distribution as a sum of two terms:

$$M(r) = \frac{M_l r^2}{(r+a)^2} + \frac{M_d r^2}{(r+d)^2}, \quad (8)$$

where the first term corresponds to mass density in equation (7), and the second term, also in the form of the Hernquist model, is included to study the possible presence of dark matter. Although the Hernquist model has a finite total mass, it can be used to approximate an isothermal halo when the scale length d is sufficiently large (Dubinski & Carlberg 1991). However, M_d should not be taken as the total mass of the dark component in this application, but merely as a parameter.

In order to compare with the Hα rotation curve of the dust lane, we write down the circular velocity of the model:

$$V_{\rm circ}(r) = \sqrt{\frac{GM_l r}{(r+a)^2} + \frac{GM_d r}{(r+d)^2}}. \quad (9)$$

If no dark matter is present, the peak circular velocity is $V_{\rm circ}(a) = \sqrt{GM_l/4a}$.

We further assume that the intrinsic stellar rotation curve is

$$V_{\rm rot}(r) = \frac{v_0 r}{(r^2 + r_0^2)^{1/2}}, \quad (10)$$

which is asymptotically flat at large radii ($r > r_0$). The projected rotation V_s along the line of sight is

$$V_s(R) = \frac{2R}{\Sigma(R)} \int_R^\infty \frac{\rho V_{\rm rot}}{\sqrt{r^2 - R^2}} dr, \quad (11)$$

where R is the projected radius on the sky, and $\Sigma(R)$ is the projected surface mass density

$$\Sigma(R) = 2 \int_R^\infty \frac{\rho r}{\sqrt{r^2 - R^2}} dr. \quad (12)$$

We determine v_0 and r_0 by fitting equation (11) to the PN major axis rotation curve. The best parameters are $v_0 = 133 \pm 14$ km s^{-1} and $r_0 = 5.5$ kpc. The projected rotation velocity is plotted in Figure 16 along with the PN data. No effort is made to correct for the inclination of the galaxy since we are probably seeing the galaxy edge on (see § 7).

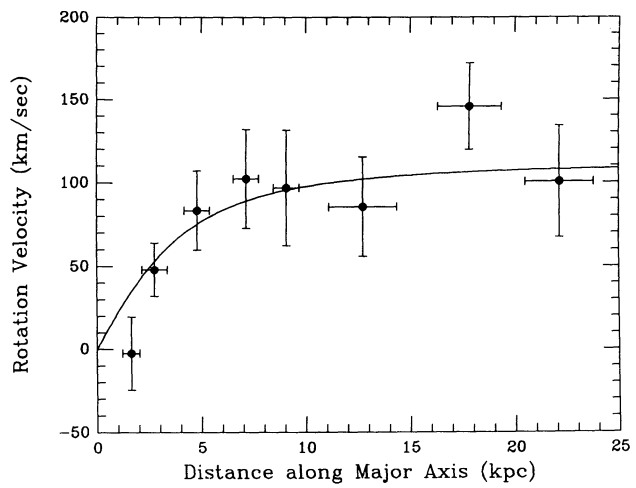

FIG. 16.—The PN major axis rotation curve along with the best-fitting model given in the text.

Given the mass model and the rotation curve, the velocity dispersion σ in equation (6) can be solved analytically (Hui 1992). The projected velocity dispersion is calculated through the line-of-sight second velocity moment:

$$\overline{V_{\rm los}^2}(R) = \frac{2}{\Sigma(R)} \int_R^\infty \left(\sigma^2 + V_{\rm rot}^2 \frac{R^2}{r^2}\right) \frac{\rho r}{\sqrt{r^2 - R^2}} dr. \quad (13)$$

The projected velocity dispersion follows

$$\sigma_s^2(R) = \overline{V_{\rm los}^2} - V_s^2. \quad (14)$$

In a self-consistent model, $\sigma_s(R)$ depends on two parameters, a and M_l; if a dark halo is included, the unknowns increase to four: a, M_l, d, and M_d.

6.2. *Central Mass-to-Light Ratio: Self-Consistent Model*

We first assume that the luminous matter is self-gravitating. In this case, the scale length of the mass distribution is set by the effective radius of the de Vaucouleurs law. According to D79, $r_e = 5.18$ kpc, and thus $a = 2.85$ kpc. The only free parameter of the model, M_l, is then determined to be $1.56 \pm 0.04 \times 10^{11}\ M_\odot$ by fitting the model to the velocity dispersion inside 1.5 kpc with a least-squares procedure. The fit is excellent (Fig. 17).

The total luminosity of NGC 5128 is $V_0 = 5.87$, and its intrinsic color is $(B-V)_0 = 0.84$ (D79). Adopting a distance modulus of $\mu = 27.73$ (Paper I), we have $L_V = 4.74 \times 10^{10}\ L_\odot$ and $L_B = 3.98 \times 10^{10}\ L_\odot$ (assuming $M_{\odot V} = 4.83$ and $M_{\odot B} = 5.48$; Allen 1976). Given the total luminous mass $M_l = 1.56 \times 10^{11}\ M_\odot$, then the mass-to-light ratio is $M/L_B = 3.9$ and $M/L_V = 3.3$. These values fit comfortably into the $M/L - L$ relationship of elliptical galaxies (see Fig. 7, Kormendy 1987) for $M_B = -20.80$, the brightness of the galaxy.

The Hα rotation curve of the dust lane is derived by fitting a series of inclined rings to the observed two-dimensional gas velocity field (NBT). Figure 18 plots the model circular velocity, scaled to the minor axis using the apparent axial ratio $e = 0.8$. It is to be compared with the observed Hα rotation curve of NBT (Fig. 9*b*). Notice NBT adopted a Cen A distance of 3 Mpc. The observed rotation curve matches the model between 1.5 and 4.3 kpc. The fact that the mass distribution

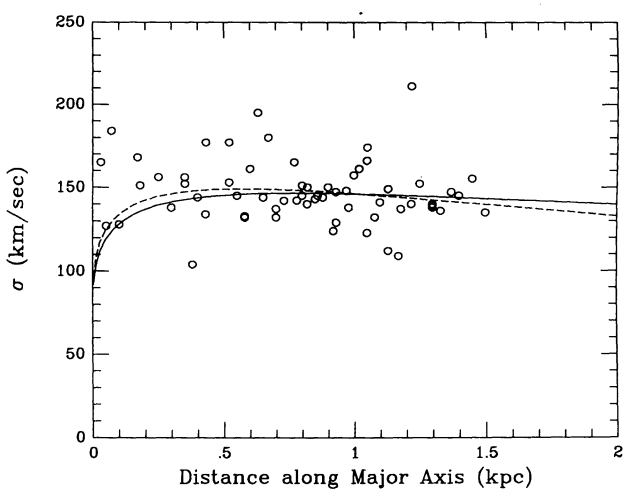

FIG. 17.—Comparison between the velocity dispersion from the absorption spectra and the models. The dashed line is for the self-consistent model, and the solid line is for the model including a dark component. The data are taken from Table 2 of WSFW. The scatter of the data reflects the measurement error.

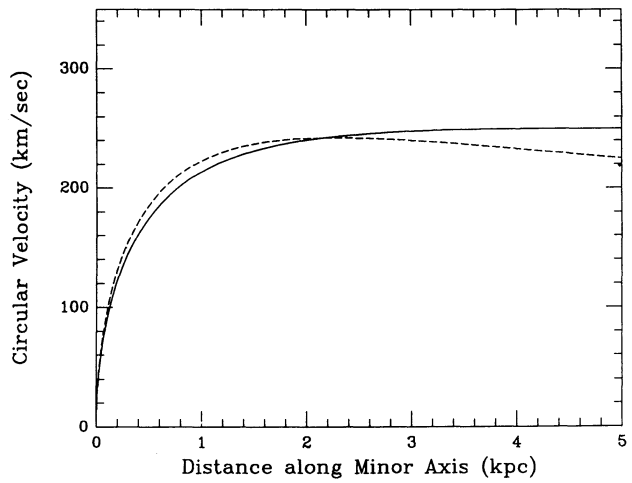

FIG. 18.—The model circular velocity. The dashed line is for the self-consistent model, and the solid line is for the model with a dark component.

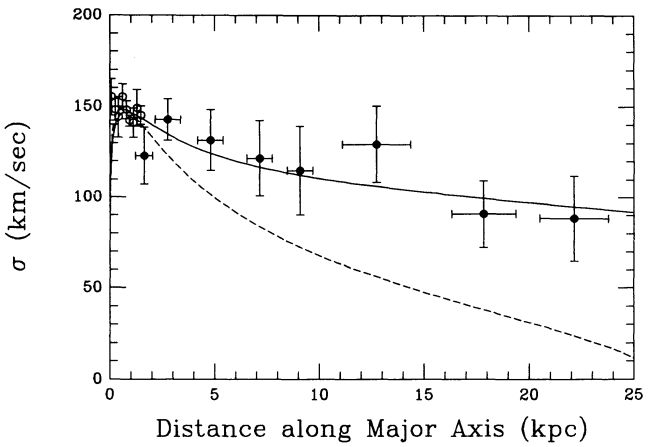

FIG. 19.—The PN velocity dispersion compared with the model predictions. (*Dashed line*) Isotropic self-consistent model; (*solid line*) two-component model as described in the text.

determined by an isotropic model predicts the gas rotation curve correctly suggests that the stellar velocity dispersion is close to isotropic in the inner region, and the derived central mass-to-light ratio is real. It also implies that the dust lane is in equilibrium with the elliptical main body, and the gas orbits are largely circular between 1.5 and 4.3 kpc.

Inside 1.5 kpc, the Hα rotation curve rises more slowly than the model. Similar phenomena are found in many early-type galaxies harboring cold gas (Bertola et al. 1991). NBT suggested a central hole in the gas emission or the decreasing inclination of the nearly edge-on disk as the two most likely explanations. We note that this could also be caused by the dust obscuration in the central region.

Based on the position-velocity map of the H I 21 cm emission, van Gorkom et al. (1990) derived a total galactic mass of $1.75 \times 10^{11}\ M_{\odot}$ (scaled to 3.5 Mpc), using the de Vaucouleurs law mass distribution. The ~10% difference between the H I results and ours could be attributed to a higher peak rotation velocities in the H I data and the difference between the de Vaucouleurs law and the Hernquist law.

6.3. *Halo Mass Distribution*

At large radii, the velocity dispersion profile predicted by the self-consistent isotropic model decreases faster than the PN velocity dispersion (Fig. 19, *short dashed line*), suggesting that a constant mass-to-light ratio model cannot fit to the observed PN velocity dispersion profile. Further evidence can be found by comparing the PN velocities with the local escape velocity in the self-gravitating Hernquist potential (Hernquist 1990):

$$V_e = \sqrt{\frac{2GM_l}{(r+a)}}\,. \tag{15}$$

Figure 20 plots the PN radial velocities as a function of the radius on the sky. Also shown is the local escape velocity. Notice that because of the projection effect, the PN velocities and their radii in space should be larger than the observed quantities. At $r > 10$ kpc, there are eight PNs whose velocities are larger than the local escape velocity. A careful check of the spectra of these objects confirms that they all have well-defined [O III] λ5007 line profiles, and the measured velocities are accurate to ± 4 km s^{-1}. Their presence suggests the existence of a dark halo.

However, it is notable that all eight PNs are on the southwest side of the galaxy. This could simply be due to the fact that the number of PNs on the southwest side is larger than that on the northeast side, but it could also indicate that the PN kinematics has not yet reached an equilibrium state. The light distribution of the NGC 5128 elliptical body is disturbed. There are not only shells, but also distinctive faint "plumes" along both ends of the photometric major axis at larger radii. These plumes are probably in the process of settling down since the last merger event. The observed PNs along the major axis beyond 10 kpc, in fact, project onto these plumes, though it is difficult to determine the percentage of the PNs in the area that actually come from them. If the majority of the halo PNs are still in a nonequilibrium state, our study of the halo mass distribution is compromised.

We adopt the two-component mass model of equation (8) to fit the halo PN velocity dispersions. There are four parameters in the model: two scale lengths, the total luminous mass M_l, and the parameter M_d. While the scale length of the luminous component is set by the de Vaucouleurs law, the others are determined by fitting the isotropic model to the combined

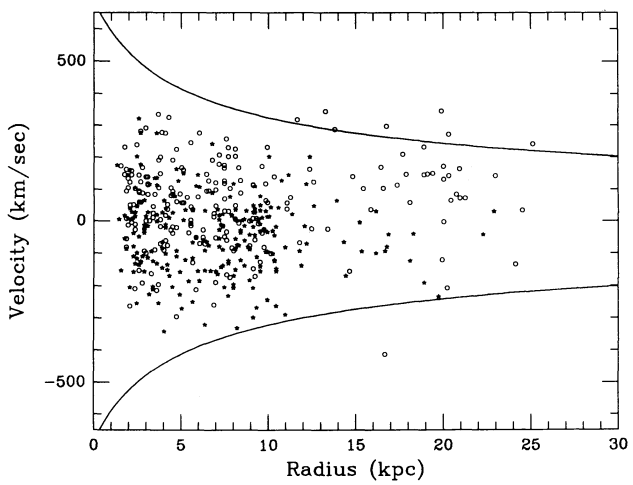

FIG. 20.—PN velocity vs. radius. The circles are PNs on the southwest side of the rotation axis, and the stars are PNs on the northeast side. The solid lines mark the position of the local escape velocity.

velocity dispersion profile of the long-slit spectra in the inner 1.5 kpc and the PN velocity dispersion between 2 and 22 kpc. The best-fitting model yields: $M_l = 1.24 \times 10^{11}\ M_\odot$, $M_d = 9.49 \times 10^{11}\ M_\odot$, and $d = 27.5$ kpc. The total luminous mass here is smaller than the value $M_l = 1.56 \times 10^{11}\ M_\odot$ derived in the self-consistent model, since we allow the dark mass density to vary continuously toward the center of the galaxy so that it does not have a hollow core. The total mass distribution and its two components are plotted in Figure 21*a*, and the mass-to-light ratio as a function of radius is given in Figure 21*b*. The M/L_B ratio increases from 3.5 at the center to 10 at 25 kpc. The total mass of the galaxy is $3.1 \times 10^{11}\ M_\odot$ within 25 kpc. The model velocity dispersion is shown in Figures 17 and 19 as the solid line. The predicted circular velocity is plotted in Figure 18. Given the relative small difference between the self-consistent model and the two-component model inside 5 kpc, the observed disk rotation curve cannot distinguish between them. However, the recently detected H I ring at 15 kpc has an intrinsic rotation of approximately 250 km s^{-1} (Schiminovich et al. 1994), which is consistent with the circular velocity of $\sim$245 km s^{-1} predicted by the two-component model.

Because the Hernquist model has a finite total mass, it is interesting to compare it with an isothermal halo,

$$\rho(r) = \frac{\rho_0}{1 + (r/D)^2}\,, \tag{16}$$

which is widely used in modeling the dark halo of spirals. We found that the dark halo in our model (*dotted curve* in Fig. 21*a*) can be approximated by an isothermal halo with $D = 2$ kpc and $\rho_0 = 0.193\ M_\odot\ \mathrm{pc}^{-3}$, which is shown as the short-long–dashed curve in the figure. The two mass distributions are identical within 25 kpc.

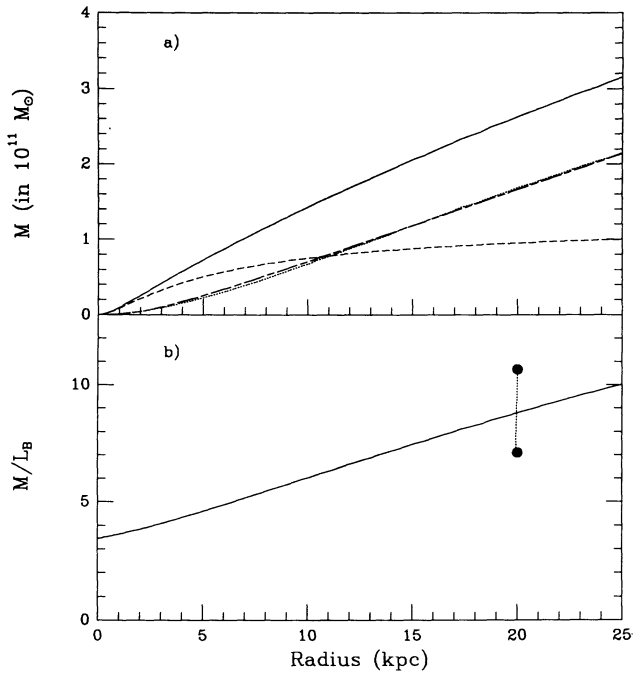

FIG. 21.—(*a*) Mass distribution as a function of radius (*solid curve*). There are two components: the luminous component (*short-dashed curve*) and the dark component (*dotted curve*). The short-long–dashed curve is an isothermal halo which has a similar mass distribution as our dark component (see text). (*b*) Mass-to-light ratio as a function of radius. The two circles linked by a dotted line are M/L_B derived using the globular cluster velocities.

The mass-to-light ratio at large radii can be compared with the globular cluster results obtained using the projected mass estimator (Heisler, Tremaine, & Bahcall 1985)

$$M = \frac{f_{\rm pm}}{GN} \sum_i^N R_i V_i^2\,, \tag{17}$$

where R_i is the galactic radius on the sky, V_i is the line-of-sight velocity, and G is the gravitational constant. The summation is over all test particles, in this case globular clusters. The value of $f_{\rm pm}$ depends on the orbital structure of the test particles:

$$f_{\rm pm} = \begin{cases} 64/\pi\,, & \text{radial}\,; \\ 32/\pi\,, & \text{isotropic}\,; \\ 64/3\pi\,, & \text{tangential}\,. \end{cases} \tag{18}$$

The first two cases are discussed in Heisler et al. (1985). The value for tangential orbits is derived by us following their prescriptions. we calculated the galaxy mass using 81 globular cluster velocities within 20 kpc radius (Harris et al. 1988; Sharples 1988). The total mass inside this radius is $3.6 \times 10^{11}\ M_\odot$ if the globular clusters are on isotropic orbits, and $2.4 \times 10^{11}\ M_\odot$ if they are on tangential orbits. Within the same radius, the total luminosity is $L_B = 3.38 \times 10^{10}\ M_\odot$. The two dots linked by a dotted line in Figure 21*b* are the corresponding mass-to-light ratios. These two values bracket the mass-to-light ratio given by the PN velocity dispersion. This not only confirms the trend of increasing mass-to-light ratio, but also suggests that the globular clusters are on partially tangential orbits. This is not surprising given the fact that the globular clusters beyond 10 kpc are identified by their slightly fuzzy appearance. The resulting sample thus consists of extended and bright globular clusters almost exclusively, which are expected to be on low eccentricity orbits and thus to experience little tidal stripping.

The X-ray mass of the galaxy within 14 kpc (Forman, Jones, & Tucker 1985) is $8.4 \times 10^{11}\ M_\odot$, which is a factor of 4.4 higher than the value in Figure 21*a*. As noted by Knapp (1987), the higher mass given by the X-ray observations could be due to the oversimplified assumption that all elliptical galaxies have a unique temperature of 1.2×10^7 K. The lack of temperature gradient information could also contribute to the overestimate of the mass. However, preliminary results of the new *ROSAT* observation of the galaxy appear to show significantly better agreement with our mass determination (Jones 1995).

6.4. *Necessity of the Dark Halo*

It is well known that if the stellar orbits are actually more tangential than isotropic at large radii, an isotropic model overestimates the halo mass. We further test the necessity of the dark halo by applying the quadratic programming (QP) method developed by Dejonghe (1989) to search for a constant mass-to-light ratio model with anisotropic stellar orbits for the PN velocities. The method approximates the spherical distribution function as a linear combination of simple components, namely, powers of the energy E and the total angular momentum J. A large freedom in the velocity anisotropy is allowed by this approach. Since the model is spherical, which does not allow for rotation, the model was fitted into the square of the stellar velocity. A marginal constant mass-to-light ratio model is found. It is not good, yet somewhat believable. The stellar orbits are highly tangential throughout the galaxy. The mass-to-light ratio of the model is $\sim$7, compared

to the $M/L_B = 3.9$ derived in our self-consistent model. The higher mass-to-light ratio is needed to maintain the high stellar velocity in the halo. In the center, the model hides much kinetic energy in the unobservable circular motion to make the line-of-sight velocity dispersion comparable to the observation.

However, the higher mass-to-light ratio presents a problem for the observed gas rotation curve. The circular velocity of the model, which peaks at 310 km s^{-1}, is much too high for the observed Hα rotation curve which has a peak velocity of 250 km s^{-1}. We conclude that even though the model is able to make the high stellar velocity unseen in the inner region by manipulating the velocity anisotropy, it cannot hide any of its circular velocity to fit the observed gas rotation. Therefore, the constant mass-to-light ratio model is rejected by the Hα rotation curve. The dark halo is indeed necessary.

7. INTRINSIC SHAPE OF NGC 5128 AND VIEWING ANGLES

7.1. *Background*

The photometry and kinematics of a dynamically relaxed stellar system can be used to delineate its intrinsic structure. However, the deprojection is highly degenerate for triaxial galaxies. There are four unknowns: two axial ratios $\zeta = b/a$ and $\xi = c/a$ ($a > b > c$), plus two viewing angles θ and ϕ. Generally, even the combined information of the isophotal shape and the stellar velocity field is not sufficient to constrain the four-parameter space. Yet a subgroup of elliptical galaxies with a prominent dust lane offer a better opportunity. Because closed orbits are stable only in a few preferred planes in a triaxial potential, the gas disk tends to settle into these planes. The relatively simple geometry of gas disks adds strong constraints so long as they are in equilibrium with the host galaxy (Merritt & de Zeeuw 1983; de Zeeuw & Franx 1989). The photometric and kinematic properties of both the elliptical body and the dust lane provides the best hope in determining the shape of a galaxy and the viewing direction. Studies along this line have been carried out by Davies & Illingworth (1986) on NGC 1052 and by Bertola et al. (1991) on NGC 5077.

NGC 5128 is one of the best known minor axis dust lane galaxies. Many data have been accumulated on both its stellar and dust lane components, stimulating considerable discussion about its intrinsic shape and orientation (Bertola & Galletta 1978; van Albada, Kotanyi, & Schwarzchild 1982; WSFW). Although the disk appears warped at large radii, the following two factors suggest that its inner region is in fact in equilibrium with the elliptical component. First, there is no relative motion between the two components since their systemic velocities are in good agreement (Graham 1979; BTA; WSFW; § 5.1). Second, the mass distribution derived using the stellar velocity dispersion predicts the rotation curve of the dust lane (§ 6). In this section we explore the intrinsic axial ratios and viewing angles of NGC 5128 assuming that the dust lane has indeed settled into a preferred plane of a triaxial potential. To facilitate the study, we give below the relevant information provided by the previous observations, as well as the newly observed PN velocity field.

1. D79 studied the light distribution of NGC 5128 on photographic plates taken with the CTIO 4 m telescope. Their measurements show that the galaxy is round in the inner region but becomes more elongated at large radii. Its ellipticity, $\epsilon = 10[1 - (b/a)]$, increases from $\epsilon = 0.7$ at $r = 2'.6$ to $\epsilon = 2.6$ at $r = 9'$. They further commented that NGC 5128 is essentially an E2 in the radius range of 4′ to 8′. A value of $\epsilon = 2.4$ at $r = 16'.5$ measured on the high contrast print of Haynes, Cannon, & Ekers (1963) is consistent with an E2 galaxy. We will take the apparent axial ratio $e = 0.8$ for the purpose of deprojection. The position angle of the photometric major axis is at P.A. = 35° ± 3° (D79).

2. The misalignment between the rotation and the photometric minor axes is a strong evidence that NGC 5128 is triaxial. Any discussion about its intrinsic shape and viewing directions should be in the context of triaxial systems. The PN velocity field shows that the rotation axis is at P.A. = 164° or 344°. The major axis rotation is in the sense of northeast approaching and southwest receding; and the minor axis rotation is such that southeast is approaching and northwest is receding.

3. By studying both the geometry and kinematics of the compact H II regions which outline the perimeter of the dust lane, Graham (1979) concluded that they form a circular ring with a radius of 2.9 kpc. The ring has an inclination of 73° to the plane of the sky, and its line of nodes is at P.A. = 125° ± 4°, lying exactly along the photometric minor axis. The young OB stars and associations follow a similar distribution (D79). The profile of this young population is best seen on a color-coded picture of the $U-B$ index (Dufour & van den Bergh 1978).

NBT studied in detail the Hα gas velocity field observed by BTA. By fitting a series of inclined annuli to the data, they obtained, as a function of radius, the deprojected Hα rotation curve, the positions of the line of nodes, and the disk inclinations. Between 1.5 and 4.3 kpc, the P.A. of the line of nodes is in the range 125°–10° to 125° + 7° (Fig. 7*a* of NBT), and the disk inclinations vary from 73°–7° to 73 + 3° (Fig. 7*c* of NBT). Given the expected uncertainties, the line of nodes and the disk inclination of the diffuse gas velocity field are consistent with those of the H II regions given by Graham (1979). However, in the inner 1.5 kpc, the line of nodes bends continuously with decreasing radius toward the photometric major axis. At the very center, it is at P.A. = 90°. We note that the gas rotation curve rises more slowly than expected for the mass distribution determined by the elliptical component (§ 6.3) in the same region. The shallow rotation curve could be due to a central hole in the gas disk or the dust in the center. In that case, the observed apparent line nodes do not provide true information of the gas velocity field.

4. WSFW reviewed in detail the disk orientation and argued that we are viewing the disk from behind. The color-coded $U-B$ index image (Dufour & van den Bergh 1978) reveals that while the northeast half of the disk is mostly intact, the southwest side is very ragged. This suggests that the northeast side is in the front, and the southwest side is behind the elliptical component. Further evidence comes from the fact that the compact H II regions are clearly associated with the dust lane at the northeast edge, but the association is poorly defined in the southwest (Graham 1979). Considering that the southeast side of the disk is approaching while the northwest side is receding, the disk angular momentum seems to point away from us.

The main objection against this configuration comes from the H I observations. Faint H I absorptions are seen against the southwest radio lobe but not the northeast radio lobe. This argues for the dust lane being in front of the southwest radio lobe (van Gorkom et al. 1990). However, the H I absorptions occur below the southwest edge of the dust lane. The absorp-

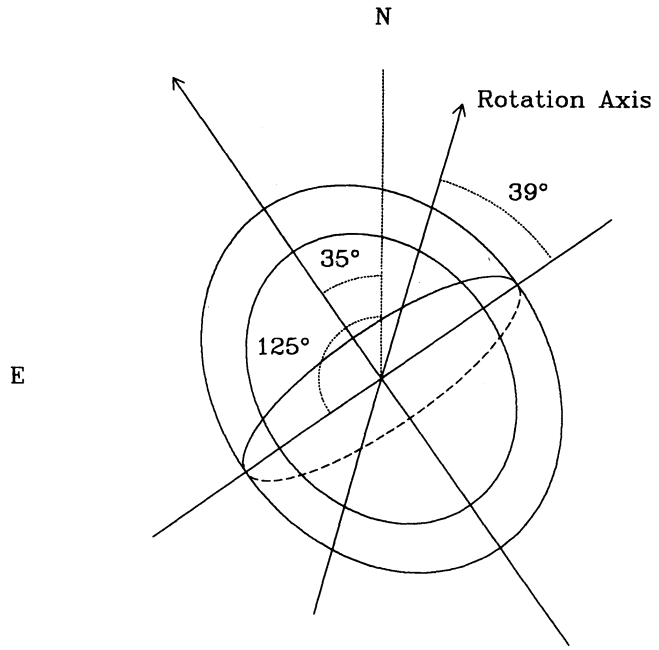

FIG. 22.—NGC 5128's configuration on the sky. The solid ellipses are the isophotes of the elliptical component. The gas disk is outlined by the solid-dashed ellipse, with the solid half representing the front side. The arrow along the rotation axis marks the direction of the angular momentum vector of the PN velocity field. The arrow on the photometric major axis points along the angular momentum of the dust lane.

tion material could come from the warped disk or some other dust seen in the southwest region (Malin, Quinn, & Graham 1983).

We summarize the above discussions with a diagram (Fig. 22). Given the position angles of the photometric major axis and the line of nodes of the disk, the dust lane lies exactly along the photometric minor axis. The disk angular momentum is therefore parallel to the photometric major axis. The line of zero rotation of the elliptical component offsets from the minor axis by 39° at P.A. = 164° or 344°. The angular momentum vectors for both the elliptical and disk components are marked in the figure.

In the following section, we show that a unique viewing direction can be found based on the disk configuration. Given the viewing angles, the axial ratios of the stellar body are allowed to vary to accommodate the observed misalignment between the stellar rotation axis and the photometric minor axis. We note that by using the constraints of both the PN velocity field and the isophotal shape, we are assuming that the dark halo has the same shape as the luminous mass.

7.2. *Axial Ratios and Viewing Angles Constrained by the Isophotal Shape*

The projection of a triaxial ellipsoid has been discussed extensively in the literature (Stark 1977; Binggelli 1980; Binney 1985). If the mass density of an elliptical galaxy is stratified on similar triaxial ellipsoids, its isophotes on the sky will be coaxial ellipses. The shape of the isophotes is determined by the axial ratios (ζ, ξ) and the viewing angles (θ, ϕ). In the following, we adopt the concepts and equations in Binney (1985) for projecting a triaxial ellipsoid onto the sky.

Let us first establish a coordinate system, with the x, y, z axes being the long, intermediate, and short axes of an ellipsoid, which is defined as

$$a_v = \sqrt{x^2 + \frac{y^2}{\zeta^2} + \frac{z^2}{\xi^2}}, \tag{19}$$

with $\zeta = b/a$, $\xi = c/a$, and $1 \geq \zeta \geq \xi$. The mass density is assumed to be a function of a_v only. The (x, y, z) system is shown in Figure 23. Also shown are the (x', y', z') coordinates related to the viewing direction, where the z'-axis is along the line of sight. We place y' in such a way that it is in the z'-z plane. Thus, x' is in the x-y plane. The two viewing angles are the two polar coordinates (θ, ϕ) of the z'-axis in the (x, y, z) system as indicated in the figure.

For a given triaxial ellipsoid characterized by parameters (ζ, ξ), the projected axial ratio is a function of viewing angles,

$$e(\theta, \phi; \zeta, \xi) = \left[\frac{A + C - \sqrt{(A-C)^2 + B^2}}{A + C + \sqrt{(A-C)^2 + B^2}}\right]^{1/2}, \tag{20}$$

where

$$\begin{aligned} A &= \frac{\cos^2\theta}{\xi^2}\left(\sin^2\phi + \frac{\cos^2\phi}{\zeta^2}\right) + \frac{\sin^2\theta}{\zeta^2}, \\ B &= \cos\theta \sin 2\phi \left(1 - \frac{1}{\zeta^2}\right)\frac{1}{\xi^2}, \\ C &= \left(\frac{\sin^2\phi}{\zeta^2} + \cos^2\phi\right)\frac{1}{\xi^2}. \end{aligned} \tag{21}$$

Generally, the photometric axes are not intrinsic principal axes in projection. The photometric minor axis is rotated by an angle ψ with respect to the projection of the intrinsic short axis on the sky,

$$\psi = \frac{1}{2}\arctan\left(\frac{B}{A-C}\right), \tag{22}$$

if the condition

$$(A-C)\cos 2\psi + B \sin 2\psi \leq 0 \tag{23}$$

is satisfied; otherwise, ψ defines the photometric major axis.

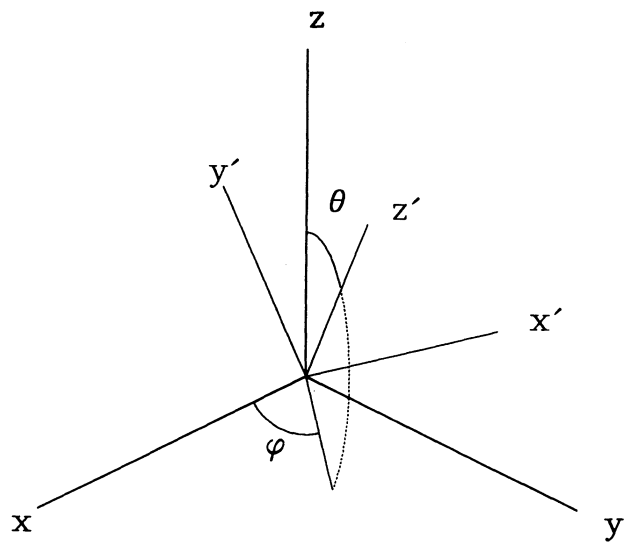

FIG. 23.—The coordinates (x, y, z) are associated with the intrinsic axes of a triaxial ellipsoid. The z' is along the line of sight, and the plane x'-y' defines the sky plane. The y' is so defined that it is in the z-z' plane. Consequently, x' is in the x-y plane. The (θ, ϕ) define the viewing direction.

Without knowing the positions of the principal axes in projection, the isophotal shape provides merely one constraint $e = e(\theta, \phi; \zeta, \xi)$, and hardly any significant limits on the intrinsic axial ratios and viewing angles. However, for a chosen pair of (ζ, ξ), the flattest system ($e = \xi$) is seen along the intermediate axis. It implies the ratio of the short axis to the long axis $\xi \leq 0.8$ for NGC 5128.

7.3. *Viewing Directions Constrained by the Dust Lane*

Much stronger constraints can be found on the orientation of the elliptical component using the dust lane configuration. For a stationary triaxial system, the gas disk settles into a plane perpendicular to either the short or long axis of the stellar figure (Merritt & de Zeeuw 1983). The alignment of the dust lane with the photometric minor axis suggests that the disk is actually in the plane of the intrinsic short and intermediate axes, and its angular momentum in space is along the intrinsic long axis. On the other hand, because the line of the nodes of the disk is along the photometric minor axis, the observed disk rotation axis is parallel to the photometric major axis. Consequently, the photometric major axis coincides with the intrinsic long axis in projection. This would be true only if the line of sight is within the principal planes of a triaxial figure: $\phi = 0°$, $\phi = 90°$, or $\theta = 90°$. The first two possibilities can be categorically excluded.

1. $\phi = 0°$.—This implies that the line of sight is in the x-z plane. Although stars are allowed to stream around both the short and long axes in a triaxial potential, the net angular momentum vector is always in the x-z plane. Therefore, when viewing the galaxy in the x-z plane, the rotation axis aligns with the photometric axes on the sky, contradicting the PN velocity field.

2. $\phi = 90°$.—The line of sight is in the y-z plane, and the gas disk is seen edge on. This cannot be true since the disk has an inclination of 73° to the plane of the sky.

The most likely situation is $\theta = 90°$, when the line of sight is in the x-y plane. In this case, the angle ϕ can be further constrained using the disk inclination of 73°, derived by assuming that the gas in the dust lane is on circular orbits. Although gas orbits are generally elongated in a triaxial potential, the orbits of the disk material between 1.5 and 4.3 kpc must be nearly circular (see § 6.2). Since the disk is in the plane of the intrinsic short and intermediate axes, its inclination restricts the viewing direction to a cone around the x-axis, $\cos 73° = \sin\theta \cos\phi$, or, by symmetry, to a similar cone around the $-x$-axis. When $\theta = 90°$, it gives $\phi = 73°$ or 107°. The second case corresponds to viewing the galaxy from the $-x$-direction. So the viewing angles are limited to essentially two points (or four by symmetry) on the unit sphere of the viewing directions. One is in the x-y plane and slightly off the intermediate axis by 17° toward the positive x-direction ($\theta = 90°$, $\phi = 73°$), and the other is in the negative x-direction ($\theta = 90°$, $\phi = 107°$).

The ambiguity can be resolved with the angular momentum vectors of the stars and disk. In a triaxial potential, stars can rotate around either the x-axis (so called x tubes) or the z-axis (Z tubes). The net angular momentum is offset from the x-axis and z-axis (Statler 1991a). For definiteness, we can assume that the photometric major axis at the northeast side is the positive x-axis and the photometric minor axis at the northwest is the positive z-axis. Since the major axis rotation is such that the northeast is approaching and the southwest is receding, the angular momentum of the Z tubes is along the z-direction. On the other hand, the minor axis rotation is in the same sense as the dust lane: the southeast approaching and the northwest receding. Thus, the angular momenta of both the X tubes and the disk are in the x-direction. If the disk angular momentum is likely pointing away from us as discussed in § 7.1, we must view the disk from behind at $\theta = 90°$, $\phi = 107°$.

7.4. *Axial Ratios*

For the given viewing direction, the photometric minor axis is also the intrinsic short axis in projection. Thus, $\psi = 0$, and

$$(A - C)\cos 2\psi + B \sin 2\psi = A - C \leq 0 . \tag{24}$$

Given the above and $B = 0$ as $\theta = 90°$, equation (20) yields

$$e(\theta, \phi; \zeta, \xi) = \left(\frac{A}{C}\right)^{1/2} . \tag{25}$$

Upon substituting A and C in equation (21), we obtain

$$\xi^2 = e^2(\sin^2\phi + \zeta^2 \cos^2\phi) . \tag{26}$$

Thus, even if the line of sight is determined, the axial ratios can only be limited to a curve in the (ζ, ξ) space. Upon substituting $\phi = 107°$, equation (26) allows the intrinsic shape to vary from being almost oblate to nearly prolate. Further constraints have to be found in the stellar kinematics. The large misalignment between the rotation axis and the photometric axes suggests that NGC 5128 is highly triaxial, so that a significant amount of both X tubes and Z tubes are present. We introduce a triaxiality parameter,

$$T = \frac{1 - \zeta^2}{1 - \xi^2} , \tag{27}$$

which is 0 for an oblate system and 1 for a prolate system. Upon solving equations (26) and (27), ζ and ξ can be expressed as

$$\zeta^2 = 1 - \frac{T(1 - e^2)}{1 - Te^2 \cos^2\phi} , \tag{28}$$

$$\xi^2 = 1 - \frac{(1 - e^2)}{1 - Te^2 \cos^2\phi} . \tag{29}$$

By constructing a family of triaxial models in the Stäckel potential, Statler has shown that when the line of sight is down the intermediate axis, the asymptotic position angle of the line of zero rotation makes an angle $\sin^{-1}(T)^{1/2}$ from the photometric minor axis (Statler 1991a; Statler 1991b). Since our viewing direction is close to the intermediate axis, we can use Statler's study to estimate the triaxial parameter T. For the observed misalignment of 39°, $T = 0.40$. Given $\phi = 107°$ and $e = 0.8$, we obtain $(\zeta, \xi) = (0.92, 0.79)$, which is fairly round yet triaxial enough to accommodate the observed stellar kinematics.

7.5. *Outer Disk Orientation*

The appearance of the dust lane is highly warped at large radii, making a $\sim 30°$ angle relative to the photometric minor axis. The investigators van Albada et al. (1982) tried to understand the disk warping by assuming that NGC 5128 has a slowly rotating triaxial figure with the dust lane on an anomalous orbit. The gas layer tilts relative to the principal plane due to the Coriolis force. However, the later observations indicate that the gas orbital motions are prograde with respect to the stellar rotation, contrary to the model prediction (WSFW).

Similarly, among six other minor axis dust lane systems observed so far, only three have the gas and stars in retrograde motion (Kormendy & Djorgovsky 1989). This suggests that the disk warping is probably a transient phenomena.

Alternatively, Tubbs (1980) proposed that NGC 5128 is a partially relaxed product of a prolate elliptical colliding with a small gas-rich galaxy. He studied the disk settling process in the context of nondissipative precession and numerically simulated the dust lane morphology. Because of the radial dependence of the precession timescale, it is expected that while the inner disk is more or less relaxed, the outer warped dust lane represents the initial inclination of the infalling disk.

If the outer dust lane indeed represents the orientation of the initial infalling disk, we can use it to predict the final destination of the dust lane in the triaxial potential determined in the previous subsection. In a stationary triaxial system, the infalling gas will settle into one of the two planes, perpendicular to either the long or the short axis. Its final destination depends on i, an angle between the initial angular momentum of the gas orbit and the long axis (Steiman-Cameron & Durisen 1982). The critical value in the x-z plane is

$$i_c = \sin^{-1}\left(\frac{1-\zeta^2}{1-\xi^2}\right)^{1/2} = \sin^{-1}\sqrt{T}\,. \qquad (30)$$

If i is less than i_c, the gas will eventually be in the y-z plane; otherwise, it will settle in the x-y plane. Since we are looking down close to the intermediate axis, a $\sim 30°$ angle between the outer disk and the intrinsic short axis implies that the initial angular momentum of the dust lane makes a $\sim 30°$ angle to the intrinsic long axis. Given the estimated triaxiality $T = 0.40$, $i_c = 39°$. So the disk indeed should settle into the y-z plane as we assumed in the study.

8. CONCLUSION AND DISCUSSION

The study of the dynamics of NGC 5128 presented in this paper yields the following main results:

1. Using multifiber spectrographs on both the AAT and CTIO 4 m telescope, we measured radial velocities of 433 PNs from the [O III] λ5007 emission line. The typical 1 σ error of the PN velocities is ± 4 km s^{-1} for the AAT data and ± 30 km s^{-1} for the CTIO data. The PNs cover the entire galaxy to 10 kpc ($2r_e$) and extend along the photometric major axis out to 20 kpc ($4r_e$).

2. The PN velocity field shows the distinctive characteristics of a triaxial potential. The rotation axis of the PN velocity field is at P.A. = 344° $\pm$ 10°, which is offset from the photometric minor axis by 39°. Between 1.5 and 12 kpc, no significant rotation axis twist is observed in the PN velocities. On the other hand, the rotation axis and the line of maximum rotation are likely not orthogonal.

3. Major axis rotation increases with radius in the inner galaxy and reaches approximately 100 km s^{-1} at 7 kpc. At larger radii, the rotation is nearly flat. The major axis velocity dispersion is ~ 143 km s^{-1} at about 3 kpc and then declines slowly throughout the halo to approximately 90 km s^{-1} at 20 kpc. The streaming motion becomes more important with increasing radius. The local V/σ reaches unity beyond 10 kpc ($2r_e$). The minor axis roation is about 50 km s^{-1} between 5 and 10 kpc, and the local V/σ is about 0.5.

4. The azimuthal variation of the velocity dispersion appears to correlate with rotation: it reaches a maximum where the largest rotation is observed and drops to a minimum at zero rotation. At 7.5 kpc, the amplitude of the modulation is about 20 km s^{-1}, while the mean velocity dispersion is 110 km s^{-1}. The correlation suggests that the projection of the rotation along the line of sight contributes to the observed dispersion modulation. It may further imply that figure rotation is not important since it does not make any contribution to the line-of-sight velocity dispersion given the nature of its solid body rotation.

5. The kinematics of the globular clusters depend on the metallicity. Given a somewhat arbitrary dividing point, [Fe/H] = -1.0, the metal-poor clusters do not show any significant rotation. However, the metal-rich group appears to have the same amplitude and direction of rotation as that of the PNs.

6. Dynamical modeling of the central stellar velocity dispersion measured from integrated light and the Hα rotation curve of the dust lane suggests that the stellar orbits are isotropic in the inner region. The central mass-to-light ratio, M/L_B, is 3.9, which fits comfortably into the $M/L - L$ relation for the galaxy's brightness.

7. By applying the isotropic Jeans equation to the observed PN major axis rotation and velocity dispersion, we find that the mass-to-light ratio increases with radius, suggesting the presence of a dark halo. The rotation velocity of the H I ring at 15 kpc confirms this conclusion. Within a 25 kpc radius, the total mass of the galaxy is 3.1×10^{11} solar masses, and $M/L_B = 10$. Similar values are obtained using the halo globular cluster data if they are on somewhat tangential orbits. Experimentation with the QP method, which allows a large freedom in velocity anisotropy, show that no constant mass-to-light ratio model can fit the major axis velocity profile and the Hα rotation curve simultaneously. Therefore, the necessity of the dark halo is further strengthened.

8. Using the information on the PN kinematics and the disk configuration, the viewing angles are estimated to be: $\theta = 90°$, $\phi = 107°$. Although in our study the uncertainties in the observed quantities were not considered, they will not change the fact that the line of sight should be close to the intermediate axis of the triaxial galaxy. The best estimated axial ratios are $\zeta = 0.92$, $\xi = 0.79$, considering the observed offset between the photometric short axis and the rotation axis.

What do these results imply for the formation and evolution of the nearest giant elliptical galaxy, NGC 5128? Hernquist (1993) recently simulated the mergers of identical spiral galaxies of a self-gravitating disk, bulge, and halo in order to better understand if such events can lead to the formation of elliptical galaxies. When we compare the observed PN kinematics to the general kinematical properties of his numerical models, similarities are indeed found. First, the fact that the rotation axis of the PNs offsets from the photometric minor axis by 39° agrees with the fact that remnants in Hernquist's simulation are triaxial and display significant misalignment between the photometric minor axis and the rotation axis. Second, the angular momentum of the remnants are mostly stored at large radii. The local V/σ could reach unity beyond 2 to 3 effective radii in the simulations. In reality, the dynamical significance of the PN rotation increases in the halo, and the local V/σ reaches approximately 1 between 10 and 15 kpc (2 to $3r_e$).

Although NGC 5128 has long been recognized as a remnant of past merger because of its conspicuous dust lane, it was suggested that the collision occurred 5×10^8 yr ago between a

giant elliptical galaxy and a small gas-rich galaxy (Tubbs 1980; Quillen, Graham, & Frogel 1993). The detection of the galaxy's shell system (Malin et al. 1983) further strengthened Tubbs's findings in view of the fact that numerical simulations can reproduce shells when a small cold disk falls into a rigid elliptical potential (Quinn 1984).

Hernquist's studies (1992, 1993) show that shells can also be formed in a major merger between two disk galaxies with comparable mass. In such an event, material in the outer disk of the spirals falls into the remnant long after the inner region of the remnant is relaxed. Thus, the formation of shells is similar to that of a small satellite accreted by a giant elliptical galaxy (Hernquist & Spergel 1992). The gas clouds in the progenitors will ultimately concentrate into the central regions of the merger remnant to form a dust lane (Hernquist & Barnes 1991). In light of the similarities between the kinematics of the PNs and the model, it is not inconceivable that NGC 5128 could also be the aftermath of a major merger. The elliptical body, the dust lane, and the shells are all formed in the same event.

However, one potential difficulty for the major merger scenario might be the appearance of the outer dust lane. The disk is highly warped at larger radii, making a 30° angle relative to the photometric minor axis. As discussed in § 7.5, in the minor merger scenario, the position angle of the outer disk represents the initial orientation of the infalling gas and dust, and the galaxy's shape as determined in § 7 is consistent with the picture in which the dust lane settles into a plane perpendicular to the intrinsic long axis.

This paper is based on part of a Ph.D thesis by X. H. at Boston University. We are indebted to Steve Meatheringham for his help at the early stage of the observation, to Tim de Zeeuw for his notes on the application of the Hernquist model, and to Herwig Dejonghe for running the QP model on the PN data. We also acknowledge useful discussions with Joss Bland-Hawthorn, Robin Ciardullo, Herwig Dejonghe, Tim de Zeeuw, Mike Fall, George Jacoby, Peter Quinn, and Tom Statler. This work was supported in part by NASA grant NAG 5-1630 and HF-1018.01-91A.

REFERENCES

Allen, C. 1976, Astrophysical Quantities (London: Athlone)
Baade, W., & Minkowski, R. 1954, ApJ, 119, 215
Bertola, F. 1987, in IAU Symp. 127, Structure and Dynamics of Elliptical Galaxies, ed. T. de Zeeuw (Dordrecht: Reidel), 135
Bertola, F., Bettoni, D., Danziger, J., Sadler, E., Sparke, L., & de Zeeuw, P. T. 1991, ApJ, 373, 369
Bertola, F., & Galletta, G. 1978, ApJ, 226, L115
Binggeli, B. 1980, A&A, 82, 289
Binney, J. 1978, MNRAS, 183, 501
———. 1985, MNRAS, 212, 767
Bland, J., Taylor, K., & Atherton, P. D. 1987, MNRAS, 228, 595 (BTA)
Burbidge, E. M., & Burbidge, G. R. 1962, Nature, 194, 367
Davies, R. L., Efstathiou, G., Fall, S. M., Illingworth, G., & Schechter, P. L. 1983, ApJ, 266, 41
Davies, R. L., & Illingworth, G. D. 1986, ApJ, 302, 234
Dopita, M. A., Jacoby, G. H., & Vassiliadis, E. 1992, ApJ, 389, 27
de Zeeuw, P. T. 1990, private communication
de Zeeuw, P. T., & Franx, M. 1989, ApJ, 343, 617
Dejonghe, H. 1989, ApJ, 343, 113
Dubinski, J., & Carlberg, R. G. 1991, ApJ, 378, 496
Dufour, R. J., & van den Bergh, S. 1978, Sky & Telescope, 56, 389
Dufour, R. J., van den Bergh, S., Harvel, C. A., Martins, D. H., Schiffer, F. H. III, Talbot, R. J., Jr., Talent, D. L., & Wells, D. N. 1979, AJ, 84, 284 (D79)
Forman, W., Jones, C., & Tucker, W. 1985, ApJ, 193, 102
Franx, M., Illingworth, G., & Heckman, T. 1989, ApJ, 344, 617
Graham, J. A. 1979, ApJ, 232, 60
Harris, H. C., Harris, G. L. H., & Hesser, J. E. 1988, in Globular Cluster Systems in Galaxies, ed. J. E. Grindlay & A. G. D. Philip (Dordrecht: Kluwer), 205
Harris, G. L. H., Geisler, D., Harris, H. C., & Hesser, J. E. 1992, AJ, 104, 613
Haynes, R. F., Cannon, R. D., & Ekers, R. D. 1983, Proc. Astron. Soc. Australia, 5(2), 241
Heisler, J., Tremaine, S., & Bahcall, J. N. 1985, ApJ, 298, 8
Hernquist, L. 1990, ApJ, 356, 359
———. 1992, ApJ, 400, 460
———. 1993, ApJ, 409, 548
Hernquist, L., & Barnes, J. E. 1991, Nature, 354, 210
Hernquist, L., & Spergel, D. N. 1992, ApJ, 399, L117
Hui, X. 1992, Ph.D. thesis, Boston Univ.
Hui, X., Ford, H. C., Ciardullo, R., & Jacoby, G. H. 1993a, ApJ, 414, 463 (Paper I)
Hui, X., Ford, H. C., Ciardullo, R., & Jacoby, G. H. 1993b, ApJS, 88, 423 (Paper II)
Illingworth, G. 1977, ApJ, 218, L43
Jones, C. 1995, private communication
Knapp, J. 1987, in IAU Symp. 127, Structure and Dynamics of Elliptical Galaxies, ed. T. de Zeeuw (Dordrecht: Reidel), 145
Kormendy, J. 1987, in IAU Symp. 127, Structure and Dynamics of Elliptical Galaxies, ed. T. de Zeeuw (Dordrecht: Reidel), 17
Kormendy, J., & Djorgovski, S. 1989, ARA&A, 27, 235
Kunkel, W. E., & Bradt, H. V. 1971, ApJ, 170, L7
Levison, H. F., & Richstone, D. O. 1987, ApJ, 314, 476
Malin, D. F., Quinn, P. J., & Graham, J. A. 1983, ApJ, 272, L5
Merritt, D. R., & de Zeeuw, P. T. 1983, ApJ, 267, L23
Möllenhoff, C., & Bender, R. 1989, A&A, 214, 61
Nicholson, R. A., Bland-Hawthorn, J., & Taylor, K. 1992, ApJ, 387, 503 (NBT)
Pelat, D., Alloin, D., & Fosbury, R. A. E. 1981, MNRAS, 195, 787
Quillen, A. C., de Zeeuw, P. T., Phinney, E. S., & Phillips, T. G. 1992, ApJ, 391, 121
Quillen, A. C., Graham, J. R., & Frogel, J. A. 1993, ApJ, 412, 550
Quinn, P. J. 1984, ApJ, 279, 596
Saglia, R. P., Bertin, G., Bertola, F., Danziger, J., Dejonghe, H., Sadler, E. M., Stiavelli, M., de Zeeuw, P. T., & Zeilinger, W. W. 1993, ApJ, 403, 567
Schiminovich, D., van Gorkom, J. H., van der Hulst, J. M., & Kasow, S. 1994, ApJ, 423, L101
Sharples, R. M. 1988, in Globular Cluster Systems in Galaxies, ed. J. E. Grindlay & A. G. D. Philip (Dordrecht: Kluwer), 545
Stark, A. A. 1977, ApJ, 213, 368
Statler, T. S. 1987, ApJ, 321, 113
———. 1991a, AJ, 102, 882
———. 1991b, private communication
Steiman-Cameron, T. Y., & Durisen, R. H. 1982, ApJ, 263, L63
Tubbs, A. D. 1980, ApJ, 241, 969
van Albada, T. S., Kotanyi, C. G., & Schwarzschild, M. 1982, MNRAS, 198, 303
van den Bergh, S. 1976, ApJ, 208, 673
van Gorkom, J. H., van der Hulst, J. M., Haschich, A. D., & Tubbs, A. D. 1990, AJ, 99, 1781
Wilkinson, A., Sharples, R. M., Fosbury, R. A. E., & Wallace, P. T. 1986, MNRAS, 218, 297 (WSFW)